FORGE

Fate Of Repository Gases

European Commission FP7

Modelling of lab and field experiments HGA EXPERIMENT

FORGE Report D4.22

	Name	Organisation	Signature	Date
Compiled	S. LEVASSEUR	University of Liege		19/10/2012
Verified	RP Shaw	BGS		8th November 2013
Approved	RP Shaw	BGS		8th November 2013

Keywords.

Mont Terri URL; HG-A experiment; Opalinus Clay; Gas flow; modelling

Bibliographical reference

S. LEVASSEUR, F. COLLIN, R. CHARLIER. 20132 Modelling of lab and field experiments HGA EXPERIMENT

FORGE Report D4.22. 57pp.

Euratom 7th Framework Programme Project: FORGE

EURATOM

Fate of repository gases (FORGE)

The multiple barrier concept is the cornerstone of all proposed schemes for underground disposal of radioactive wastes. The concept invokes a series of barriers, both engineered and natural, between the waste and the surface. Achieving this concept is the primary objective of all disposal programmes, from site appraisal and characterisation to repository design and construction. However, the performance of the repository as a whole (waste, buffer, engineering disturbed zone, host rock), and in particular its gas transport properties, are still poorly understood. Issues still to be adequately examined that relate to understanding basic processes include: dilational versus visco-capillary flow mechanisms; long-term integrity of seals, in particular gas flow along contacts; role of the EDZ as a conduit for preferential flow; laboratory to field up-scaling. Understanding gas generation and migration is thus vital in the quantitative assessment of repositories and is the focus of the research in this integrated, multi-disciplinary project. The FORGE project is a pan-European project with links to international radioactive waste management organisations, regulators and academia, specifically designed to tackle the key research issues associated with the generation and movement of repository gasses. Of particular importance are the long-term performance of bentonite buffers, plastic clays, indurated mudrocks and crystalline formations. Further experimental data are required to reduce uncertainty relating to the quantitative treatment of gas in performance assessment. FORGE will address these issues through a series of laboratory and field-scale experiments, including the development of new methods for up-scaling allowing the optimisation of concepts through detailed scenario analysis. The FORGE partners are committed to training and CPD through a broad portfolio of training opportunities and initiatives which form a significant part of the project.

Further details on the FORGE project and its outcomes can be accessed at www.FORGEproject.org.

Contact details:

S. Levasseur, F. Collin, R. Charlier

Université de Liège – ArGEnCo

Secteur Géotechnologies, Hydrogéologie, Prospection géophysique (GEO³)

Institut de Mécanique et de Génie Civil, Chemin des Chevreuils 1, Bât. B52/3 B 4000

Liège 1 - Sart Tilman

Belgique

Tél.: 04/366.93.34

Fax: 04/366.93.26

E-mail severine.levasseur@ulg.ac.be; f.collin@ulg.ac.be; robert.charlier@ulg.ac.be

www.argenco.ulg.ac.be

Faculté des Sciences Appliquées
Département d'Architecture, Géologie, Environnement & Constructions
Secteur GEO³
Prof. R. CHARLIER

FORGE – WP4
TASK 4.3: Modelling of lab and field experiments
HGA EXPERIMENT

Technical report

19/10/2012

S. Levasseur, F. Collin, R. Charlier

severine.levasseur@ulg.ac.be, f.collin@ulg.ac.be, robert.charlier@ulg.ac.be

Université de Liège – ArGEnCo
www.argenco.ulg.ac.be
Secteur Géotechnologies, Hydrogéologie, Prospection géophysique (GEO³)

Institut de Mécanique et de Génie Civil, Chemin des Chevreuils 1, Bât. B52/3 B 4000
Liège 1 - Sart Tilman– Belgique
Tél.: 04/366.93.34 ; Fax: 04/366.93.26
E-mail : Robert.Charlier@ulg.ac.be

Table of content

1 HGA EXPERIMENT OBJECTIVES AND MODELLING PLAN 7

2 CONSTITUTIVE MODELS 8

2.1 Mechanical anisotropy 8

2.2 Hydraulic anisotropy 15

2.3 Balance equations 16

3 MODEL PARAMETERS IDENTIFICATION 16

3.1 Mechanical parameter estimation from triaxial tests 16

3.2 Hydraulic parameters 19

4 2D MODELLING OF TUNNEL EXCAVATION 20

4.1 Geometry, boundary conditions and loading description 20

4.2 Hydromechanical parameters 23

4.3 Qualitative analysis of numerical results 24
4.3.1 Influence of anisotropic settings on global behaviour 24
4.3.2 Interpretation of numerical results 32

4.4 Complementary investigations for quantitative analysis 33
4.4.1 Mesh sensitivity around HGA borehole 34
4.4.2 Influence of the lateral large gallery on HGA modelling 35
4.4.3 Influence of the tectonic fault 39
4.4.4 Introduction of an artificial EDZ around HGA borehole 40

4.5 Calibration on experimental results 43
4.5.1 Influence of EDZ properties 43
4.5.2 Influence of undamaged Opalinus Clay properties 47
4.5.3 Final calibrations 49

5 CONCLUSIONS 56

6 REFERENCES 56

List of figures

Figure 1: General layout of the HGA gallery with instrumentation boreholes (Trick et al., 2007)..... 7

Figure 2: General test plan of the HGA experiment (Trick et al., 2007) 8

Figure 3: Transformation of the global axis $(\underline{E}_1, \underline{E}_2, \underline{E}_3)$ into anisotropic axes $(\underline{e}_1, \underline{e}_2, \underline{e}_3)$. 9

Figure 4: Yield surface of the Drucker-Prager criterion in the deviatoric plane. Comparison with the Mohr-Coulomb yield surface. 12

Figure 5: Schematic view of the cohesion evolution as a function of the angle between the normal vector to bedding plane and the direction of major principal stress. 13

Figure 6: Hardening/softening hyperbolic relation for two values of coefficient Bp 14

Figure 7: Orientation of bedding with respect to the loading direction in P-, S- and Z- samples 17

Figure 8: Triaxial results under 4 different confinement pressures σ_3 for three different inclinations of the bedding plane with respect to the loading direction σ_1 17

Figure 9: Failure criteria in (p, q) plane for three different inclinations of the bedding plane with respect to the loading direction σ_1..... 18

Figure 10: Triaxial tests calibrations under 4 different confinement pressures σ_3 for three different inclinations of the bedding plane with respect to the loading direction σ_1..... 19

Figure 11: Schematic view of the orientation of the HGA gallery with respect to bedding plane. 20

Figure 12: Boundary conditions of the 2D plane strain model. 21

Figure 13: Hydromechanical loading (subtask 1) 21

Figure 14: Projection of the sensor location in the 2D modelling section. 22

Figure 15: Experimental measurements around HGA tunnel 22

Figure 16: Effect of initial stress anisotropy on horizontal and vertical stresses and plastic indicator in purely mechanical modelling at the end of excavation phase..... 24

Figure 17: Effect of initial stress anisotropy on water pressure and plastic indicator in coupled hydro-mechanical modelling at the end of excavation phase 25

Figure 18: Effect of Young modulus anisotropy on horizontal and vertical stresses and plastic indicator in purely mechanical modelling at the end of excavation phase..... 26

Figure 19: Effect of cohesion anisotropy on horizontal and vertical stresses and plastic indicator in purely mechanical modelling at the end of excavation phase..... 26

Figure 20: Effect of cohesion anisotropy on water pressure and plastic indicator in coupled hydro-mechanical modelling at the end of excavation phase 27

Figure 21: Simultaneous effect of initial stress, Young modulus and cohesion anisotropies on horizontal and vertical stresses, plastic indicator and deformed mesh in purely mechanical modelling at the end of excavation phase 27

Figure 22: Simultaneous effect of mechanical anisotropies on hydro-mechanical modelling with isotropic hydraulic conditions at the end of excavation phase and after 10 months of ventilation 29

Figure 23: Effect of permeability anisotropy on water pressure and plastic indicator in coupled hydro-mechanical modelling at the end of excavation phase 29

Figure 24: Simultaneous effect of mechanical anisotropies on hydro-mechanical modelling with anisotropic hydraulic conditions at the end of excavation phase and after 10 months of ventilation 31

Figure 25: Simultaneous effect of mechanical anisotropies on water pressure field with anisotropic hydraulic conditions and exaggerated permeability anisotropic ratio after 10 months of ventilation 31

Figure 26: (a) Picture of HGA borehole; (b) Schematic view of damage 33

Figure 27: Water pressure evolution with time in HG-A3 borehole – first comparison between experimental measurements and numerical results 33

Figure 28: Pore pressure evolution after excavation depending of mesh size 34

Figure 29: Comparison of water pressure evolutions with time at 50cm to tunnel wall in the horizontal direction (HG-A3) for 4 different meshes 34

Figure 30: Views of HGA microtunnel and Gallery04 in Mont Terri URL 35

Figure 31: Simulation of Gallery04 before HGA drilling – plastic indicator and water pressure evolutions after excavation and after 8 months of ventilation 36

Figure 32: Pore pressure evolutions around gallery04 and HGA microtunnel 37

Figure 33: Saturation degree evolutions around HGA microtunnel (modelling accounting gallery effect) 37

Figure 34: Plastic indicator evolutions around gallery04 and HGA microtunnel 38

Figure 35: Influence of tectonic fault around HGA borehole 39

Figure 36: Excavation Damaged Zone definition around HGA borehole based as an ellipsoid including area around tunnel where plastic indicator PI > 0.5 40

Figure 37: Influence of EDZ at the end of excavation phase 41

Figure 38: Influence of EDZ after ventilation phase 42

Figure 39: Influence of EDZ size on water pressure and displacement evolutions with time . 44

Figure 40: Influence of Young modulus in EDZ on water pressure and displacement evolutions with time 45

Figure 41: Influence of permeability in EDZ on water pressure and displacement evolutions with time 46

Figure 43: Influence of vapour mass transfer coefficient on water pressure evolutions with time 48

Figure 44: Influence of permeability outside EDZ on water pressure evolutions with time ... 49

Figure 45: Calibration of B-A03PE1 water pressure evolutions with time 50

Figure 46: Calibration of B-A03PE2 water pressure evolutions with time 50

Figure 47: Calibration of B-A03PE3 water pressure evolutions with time 51

Figure 48: Calibration of B-A02PE2 water pressure evolutions with time 51

Figure 49: Calibration of water pressure and displacements evolutions with time (mainly based on pore water pressure evolution) 52

Figure 50: Calibration of water pressure and displacements evolutions with time (mainly based on displacement evolutions)..... 53

Figure 51: Final calibration of water pressure and displacements evolutions with time 54

List of tables

Table 1: Young modulus identification on triaxial test with bedding orientation 18

Table 2: Hydraulic characteristics..... 19

Table 3: Opalinus Clay parameters 23

Table 4: Tectonic fault characteristics 39

Table 5: Initial calibrations 43

Table 6: Young modulus and Permeability calibrations 49

Table 7: Calibrated Opalinus Clay parameters 55

1 HGA experiment objectives and modelling plan

The objective of the HGA experiment is to investigate the hydro-mechanical evolution of a backfilled and sealed tunnel section. In particular, the goals concern:

- the understanding of the generation and the behaviour evolutions of an Excavation Damaged Zone (EDZ) in Opalinus Clay;

- the upscaling of hydraulic conductivity determination from the lab test to the tunnel scale;

- the investigation of self-sealing processes;

- the estimation of gas leakage rates.

The geometry of the problem consists in a tunnel of 13m in length and 1.035m in diameter drilled in Opalinus Clay. More than 20 observation boreholes have been drilled parallel and oblique to the microtunnel axis and equipped with multipacker piezometer systems, inclinometer chains, chain deflectometers and stress cells to monitor the correspondent parameters in the host rock (pore water pressure, total stress and displacements – cf. Figure 1). After excavation, the micro-tunnel has also been instrumented with surface extensometers, strain gages, time domain reflectometers (TDRs), piezometers and geophones.

The test plan consists in the drilling and instrumentation of the boreholes (Phase 0), the excavation of the microtunnel followed by backfilling and sealing (Phase 1), installation and inflation of the megapacker (Phase 2), hydraulic constant pressure and constant rate injection tests (Phase 3), gas injection tests (Phase 4) and a second hydraulic test series (Phase 5) (cf. Figure 2 – Trick et al., 2007).

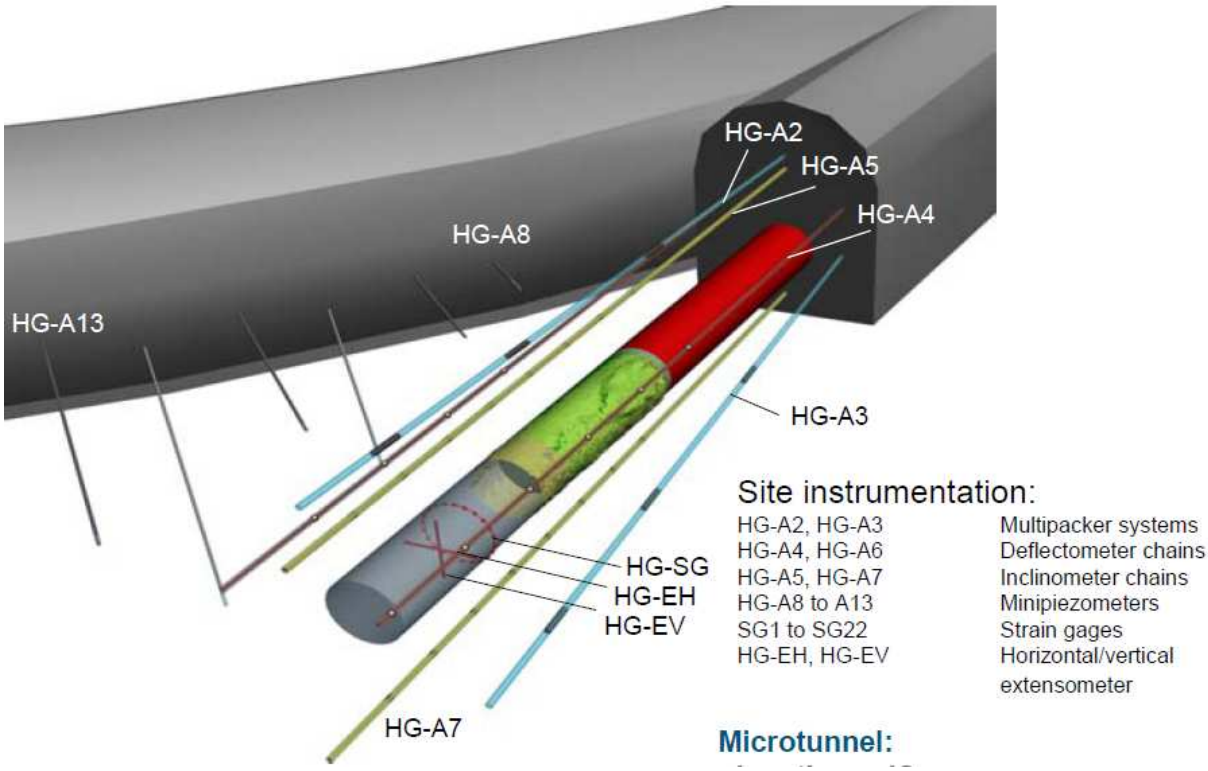

Figure 1: General layout of the HGA gallery with instrumentation boreholes (Trick et al., 2007)

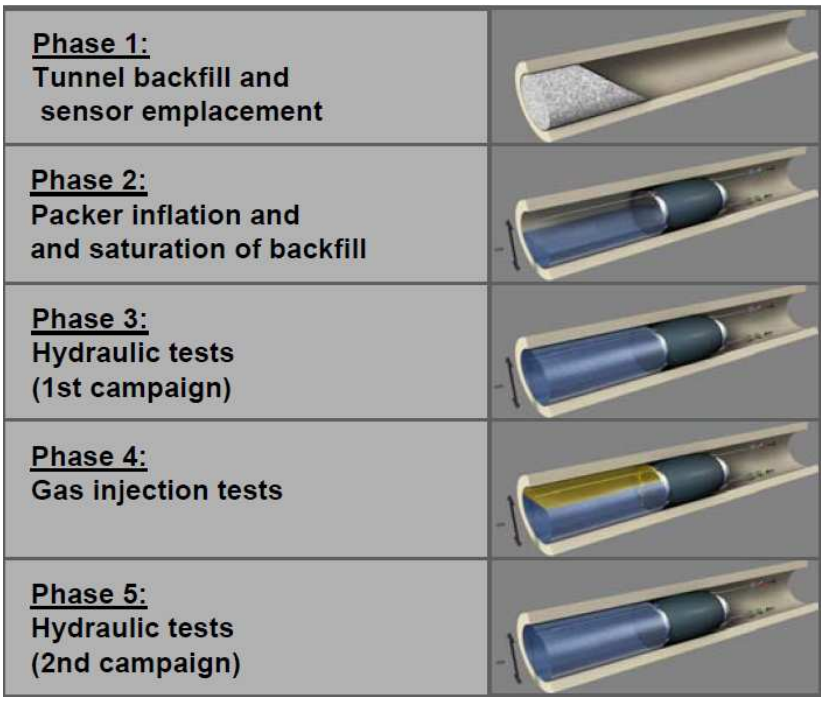

Figure 2: General test plan of the HGA experiment (Trick et al., 2007)

In the framework of the Workpackage 4 (WP 4) – Task 4.3 (Modelling of lab and field experiments), the global approach of the phenomena are divided in the following four stages (I. Gaus, G.W. Lanyon, P. Marschall, J. Rueedi, 19 Nov. 2009, oral communication):

SubTask 1: *Modelling of tunnel excavation* considering mechanical behaviour of Opalinus Clay (including anisotropy and suction), development of EDZ.

SubTask 2: *Modelling of water injection* considering resaturation, evolution and role of EDZ, interpretation of long term injection tests and self-sealing.

SubTask 3*: Modelling of the gas injection* including the design and the prediction of gas injection phase, the model calibration, the test interpretation and the interpretation of the second set of hydrotests.

SubTask 4: *Insight modelling and upscaling.*

In this context, ULg have carried out some particular numerical tools that are described in the following.

2 Constitutive models

Opalinus Clay is well-known to have a non-negligible anisotropic behaviour. Constitutive models taking into account this anisotropy have been developed.

2.1 Mechanical anisotropy

The model uses elastic cross-anisotropy coupled with an extended Drucker-Prager hardening plasticity model. The plastic yield limit considers that the material cohesion depends on the angle between major principal stress and the bedding orientation.

The elasto-plasticity principle (concept of a loading surface f in the stress space which limits the region of elastic deformation) allows that the total strain rate $\dot{\varepsilon}_{ij}$ be split into elastic $\dot{\varepsilon}_{ij}^{e}$ and plastic $\dot{\varepsilon}_{ij}^{p}$ components:

$$\dot{\varepsilon}_{ij} = \dot{\varepsilon}_{ij}^{e} + \dot{\varepsilon}_{ij}^{p} \tag{2-1}$$

Because of elastic anisotropy, the elasto-plastic stress-strain relations are more convenient to be expressed in the anisotropic axis, as indicated by the star in exponent ($\sigma_{ij}'^{*}$ and ε_{ij}^{*})

$$\dot{\sigma}_{ij}'^{*} = C_{ijkl}\dot{\varepsilon}_{kl}^{*} \tag{2-1}$$

where C_{ijkl} is the elasto-plastic constitutive matrix.

In the more general situation, the reference axes do not coincide with the axes of anisotropy and the expression of $\sigma_{ij}'^{*}$ and ε_{ij}^{*} can be obtained from σ_{ij}' and ε_{ij} expressed in the system of reference through the following transformation:

$$\sigma_{ij}'^{*} = R_{ki}R_{lj}\sigma_{kl}' \quad ; \quad \varepsilon_{ij}^{*} = R_{ki}R_{lj}\varepsilon_{kl} \tag{2-2}$$

where R_{ij} is the ij component of the rotation matrix:

$$R = \begin{bmatrix} \cos\alpha\cos\varphi & \sin\alpha\cos\varphi & \sin\varphi \\ -\sin\alpha\cos\theta - \sin\theta\sin\varphi\cos\alpha & \cos\alpha\cos\theta - \sin\theta\sin\varphi\sin\alpha & \sin\theta\cos\varphi \\ \sin\theta\sin\alpha - \cos\alpha\sin\varphi\cos\theta & -\sin\varphi\sin\alpha\cos\theta - \sin\theta\cos\alpha & \cos\varphi\cos\theta \end{bmatrix} \tag{2-3}$$

in which α is the rotation angle around the axes $\underline{E}_3$ (rotation in the $(\underline{E}_1, \underline{E}_2)$) plane, the angles φ and θ define the rotations around the axes $\underline{e}'_2$ and $\underline{e}_1$, respectively (Figure 3). The positive direction of rotation is counter-clockwise. $(\underline{E}_1, \underline{E}_2, \underline{E}_3)$ and $(\underline{e}_1, \underline{e}_2, \underline{e}_3)$ are the reference axes and the anisotropic axes, respectively.

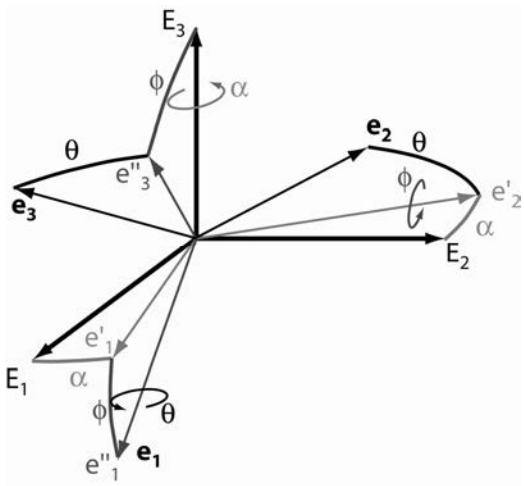

Figure 3: Transformation of the global axis $(\underline{E}_1, \underline{E}_2, \underline{E}_3)$ into anisotropic axes $(\underline{e}_1, \underline{e}_2, \underline{e}_3)$.

At the end of each step of computation, the stress and strain obtained in the anisotropic axes (σ'^{*}_{ij} and ε^{*}_{ij}) are re-transformed to be expressed in the global axes (σ'_{ij} and ε_{ij}):

$$\sigma'_{ij} = R_{ik} R_{jl} \sigma'^{*}_{kl} \quad ; \quad \varepsilon_{ij} = R_{ik} R_{jl} \varepsilon^{*}_{kl} \tag{2-4}$$

Elastic anisotropy

$\dot{\varepsilon}^{*e}_{ij}$ is the ij strain rate component that does not modify the hardening state of the material. $\dot{\varepsilon}^{*e}_{ij}$ is linked to stress rate through the Hooke law :

$$\dot{\varepsilon}^{*e}_{ij} = D^{e}_{ijkl} \dot{\sigma}'^{*}_{kl} \tag{2-5}$$

The D^{e}_{ijkl} matrix deals with anisotropic elasticity. Considering the requirement of symmetry of the stiffness matrix, the anisotropic elasticity needs a maximum of 21 independent parameters to be fully described. However, axes of symmetry in the structure of many materials limit the number of independent parameters. An anisotropy induced by three orthogonal structural directions, usually called *orthotropy*, requires 9 parameters to define the elastic matrix, as follow:

$$D^{e}_{ijkl} = \begin{bmatrix} \frac{1}{E_1} & -\frac{\nu_{21}}{E_2} & -\frac{\nu_{31}}{E_3} & & & \\ -\frac{\nu_{12}}{E_1} & \frac{1}{E_2} & -\frac{\nu_{32}}{E_3} & & & \\ -\frac{\nu_{13}}{E_1} & -\frac{\nu_{23}}{E_2} & \frac{1}{E_3} & & & \\ & & & \frac{1}{2G_{12}} & & \\ & & & & \frac{1}{2G_{13}} & \\ & & & & & \frac{1}{2G_{23}} \end{bmatrix} \tag{2-6}$$

The symmetry of the stiffness matrix imposes that

$$\frac{\nu_{21}}{E_2} = \frac{\nu_{12}}{E_1} \quad ; \quad \frac{\nu_{31}}{E_3} = \frac{\nu_{13}}{E_1} \quad ; \quad \frac{\nu_{23}}{E_2} = \frac{\nu_{32}}{E_3} \tag{2-7}$$

By inversing the matrix D^{e}_{ijkl}, the elastic relation is:

$$\dot{\sigma}'^{*}_{ij} = C^{e}_{ijkl} \dot{\varepsilon}^{*e}_{kl} \tag{2-8}$$

with

$$C_{ijkl}^{e} = \begin{bmatrix} \frac{1-\nu_{23}\nu_{32}}{E_2E_3\det} & \frac{\nu_{21}+\nu_{31}\nu_{23}}{E_2E_3\det} & \frac{\nu_{21}\nu_{32}+\nu_{31}}{E_2E_3\det} & & & \\ \frac{\nu_{12}+\nu_{13}\nu_{32}}{E_1E_3\det} & \frac{1-\nu_{13}\nu_{31}}{E_1E_3\det} & \frac{\nu_{32}+\nu_{31}\nu_{12}}{E_1E_3\det} & & & \\ \frac{\nu_{13}+\nu_{23}\nu_{12}}{E_1E_2\det} & \frac{\nu_{23}+\nu_{21}\nu_{13}}{E_1E_2\det} & \frac{1-\nu_{21}\nu_{12}}{E_1E_2\det} & & & \\ & & & 2G_{12} & & \\ & & & & 2G_{13} & \\ & & & & & 2G_{23} \end{bmatrix} \tag{2-9}$$

$$\text{and } \det = \frac{1-\nu_{31}\nu_{13}-\nu_{21}\nu_{12}-\nu_{32}\nu_{23}-2\nu_{31}\nu_{12}\nu_{23}}{E_1E_2E_3} \tag{2-10}$$

Sedimentary rocks show usually a more limited form of anisotropy. The behaviour is isotropic in the plane of bedding and the unique direction of anisotropy is perpendicular to bedding. The properties of such materials are independent of rotation about an axis of symmetry normal to the bedding plane (Graham and Houlsby, 1982). This type of elastic anisotropy, called *transverse isotropy* or *cross-anisotropy*, requires 5 independent parameters and is a particular case of Equations (2-6) and (2-9) for which:

$$\begin{cases} E_1 = E_2 = E_{//} \\ E_3 = E_{\perp} \\ \nu_{12} = \nu_{21} = \nu_{//,//} \\ \nu_{13} = \nu_{23} = \nu_{//,\perp} \\ G_{13} = G_{23} = G_{//,\perp} \\ G_{12} = G_{//,//} = \dfrac{E_{//}}{2\left(1+\nu_{//,//}\right)} \end{cases} \tag{2-11}$$

where the subscripts // and $\perp$ indicate, respectively, the direction parallel to bedding (directions 1 and 2) and perpendicular to bedding (direction 3).

Plastic anisotropy

The Drucker-Prager plastic yield limit, flow rule and consistency condition are expressed in the anisotropic axis (stress and strain components are expressed with a star exponent). This way of proceed aims at keeping the elastic matrix (needed in the development of the consistency condition) as simple as possible.

The limit between the elastic and the plastic domain is represented by a yield surface in the principal stress space. This surface corresponds to the Drucker-Prager yield surface f (Drucker and Prager, 1952):

$$f \equiv II_{\hat{\sigma}} - m\left(I_{\sigma} - \frac{3c}{\tan\phi}\right) = 0 \tag{2-12}$$

with $$m = \frac{2\sin\phi}{\sqrt{3}\left(3-\sin\phi\right)} \tag{2-13}$$

I_σ and $II_{\hat{\sigma}}$ are the first stress tensor invariant and the second deviatoric stress tensor invariant, respectively:

$$I_\sigma = \sigma'^{*}_{ii} \tag{2-14}$$

$$II_{\hat{\sigma}} = \sqrt{\frac{1}{2}\hat{\sigma}'^{*}_{ij}\hat{\sigma}'^{*}_{ij}} \quad ; \quad \hat{\sigma}'^{*}_{ij} = \sigma'^{*}_{ij} - \frac{I_\sigma}{3}\delta_{ij} \tag{2-15}$$

In Equation (2-12), the linear coefficient m between the first and the second stress invariant being independent of the third invariant (or alternatively, the Lode angle), the plastic surface is a cone in the principal stress space. The trace of this plasticity surface on the Π plane (deviatoric plane) is a circle (Figure 4).

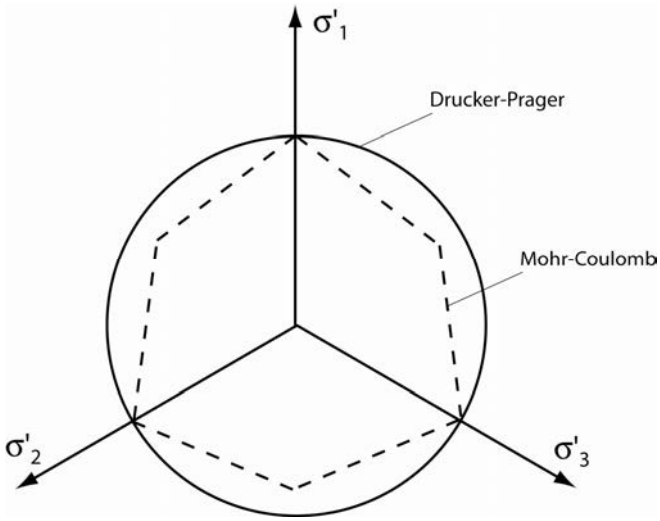

Figure 4: Yield surface of the Drucker-Prager criterion in the deviatoric plane. Comparison with the Mohr-Coulomb yield surface.

The criterion assumes that the strength of materials varies according to the orientation of the principal compressive stress with respect to the bedding plane orientation. Anisotropy of material cohesion depends on the angle between major principal stress and the normal to the bedding plane following experimental observations of Niandou et al. (1997) or failure criteria proposed for sedimentary rocks by Duveau et al. (1998), Pietruszczak and Mroz, (2001) and Pietruszczak et al. (2002).

Then, three cohesion values are defined, for major principal stress parallel ($\alpha_{\sigma_1} = 0°$), perpendicular ($\alpha_{\sigma_1} = 90°$) and with an angle of 45° ($\alpha_{\sigma_1} = 45°$) with respect to the normal to bedding plane. Between those values, cohesion varies linearly with α_{σ_1}. The mathematical expression of the cohesion is as follows (Figure 5):

$$c = \max\left[\left(\frac{c_{45°} - c_{0°}}{45°}\right)\alpha_{\sigma_1} + c_{0°} \;;\; \left(\frac{c_{45°} - c_{0°}}{45°}\right)\left(\alpha_{\sigma_1} - 45°\right) + c_{45°}\right] \tag{2-16}$$

with α_{σ_1} being the angle between the normal to the bedding plane $\vec{n}$ and the major principal stress $\vec{\sigma}'_1$:

$$\alpha_{\sigma_1} = \arccos\left(\frac{\vec{n}.\vec{\sigma}'_1}{\|\vec{n}\|\|\vec{\sigma}'_1\|}\right) \tag{2-17}$$

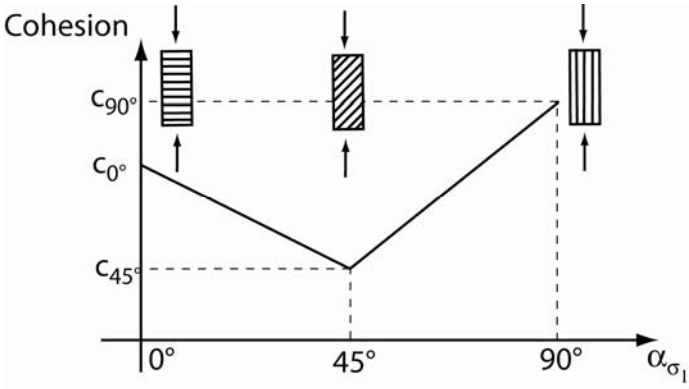

Figure 5: Schematic view of the cohesion evolution as a function of the angle between the normal vector to bedding plane and the direction of major principal stress.

In addition, a general non-associated plasticity framework is considered:

$$\dot{\varepsilon}_{ij}^{*p} = \lambda^P \frac{\partial g}{\partial \sigma'^*_{ij}} \tag{2-18}$$

with the plastic potential g defined as:

$$g \equiv II_{\hat{\sigma}} + m' I_\sigma = 0 \tag{2-19}$$

in which $$m' = \frac{2\sin\psi}{\sqrt{3}(3-\sin\psi)} \tag{2-20}$$

where ψ is the dilatancy angle. When $\psi = \phi$, $\frac{\partial f}{\partial \sigma'^*_{ij}} = \frac{\partial g}{\partial \sigma'^*_{ij}}$ and the flow rule is associated.

The plastic multiplier λ^p is obtained from the consistency condition, which states that during plastic flow the stress state stays on the limit surface:

$$df \equiv \frac{\partial f}{\partial \sigma'^*_{ij}} \dot{\sigma}'^*_{ij} + \frac{\partial f}{\partial \kappa} \dot{\kappa} = 0 \tag{2-21}$$

with κ being the hardening variable(s). The used model is a hardening Drucker-Prager model that allows hardening/softening processes during plastic flow. This is introduced via an hyperbolic variation of the friction angle and the cohesion between initial (ϕ_0 and c_0) and final (ϕ_f and c_f) values as a function of the Von Mises equivalent plastic strain ε_{eq}^p (Barnichon, 1998):

$$\phi = \phi_0 + \frac{\left(\phi_f - \phi_0\right)\varepsilon_{eq}^p}{B_p + \varepsilon_{eq}^p} \tag{2-22}$$

$$c = c_0 + \frac{\left(c_f - c_0\right)\varepsilon_{eq}^p}{B_c + \varepsilon_{eq}^p} \tag{2-23}$$

where the Von Mises equivalent plastic strain ε_{eq}^p is obtained by integration of the Von Mises equivalent plastic strain rate $\dot{\varepsilon}_{eq}^p$:

$$\varepsilon_{eq}^p = \int_0^t \dot{\varepsilon}_{eq}^p dt \quad ; \quad \dot{\varepsilon}_{eq}^p = \sqrt{\frac{2}{3}\dot{\hat{\varepsilon}}_{ij}^{*p}\dot{\hat{\varepsilon}}_{ij}^{*p}} \tag{2-24}$$

Coefficients B_p and B_c represent respectively the values of equivalent plastic strain for which half of the hardening/softening on friction angle and cohesion is achieved (Figure 6). Thus, the consistency condition given in equation (2-21) reads:

$$df \equiv \frac{\partial f}{\partial \sigma_{ij}'^*}\dot{\sigma}_{ij}'^* + \left(\frac{\partial f}{\partial \phi}\frac{d\phi}{d\varepsilon_{eq}^p} + \frac{\partial f}{\partial c}\frac{dc}{d\varepsilon_{eq}^p}\right)\dot{\varepsilon}_{eq}^p = 0 \tag{2-25}$$

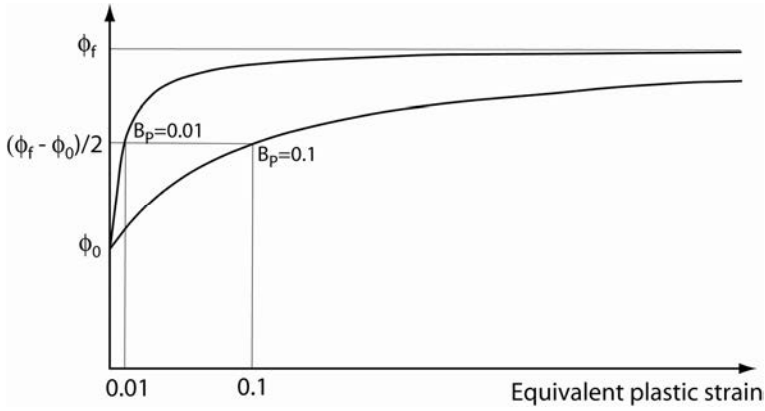

Figure 6: Hardening/softening hyperbolic relation for two values of coefficient Bp

The Von Mises equivalent plastic strain can be expressed as a function of the plastic multiplier combining Equations (2-18) and (2-24), for the specific expression of the Drucker-Prager plastic potential (2-19):

$$\dot{\varepsilon}_{eq}^p = \sqrt{\frac{2}{3}\left(\frac{\partial g}{\partial \sigma_{ij}'^*}\frac{\partial g}{\partial \sigma_{ij}'^*} - \frac{1}{3}\frac{\partial g}{\partial \sigma_{kk}'^*}\frac{\partial g}{\partial \sigma_{ll}'^*}\right)}\dot{\lambda}^P = \frac{\sqrt{3}}{3}\dot{\lambda}^P \tag{2-26}$$

Combining together the elastic relation (2-8) and expression of plastic strain gives:

$$\dot{\sigma}_{ij}^* = C_{ijkl}\left(\dot{\varepsilon}_{kl}^* - \dot{\lambda}^p \frac{\partial g}{\partial \sigma_{kl}'^*}\right) \tag{2-27}$$

That allows us to determine the plastic multiplier $\dot{\lambda}^p$:

$$\dot{\lambda}^p = \frac{\dfrac{\partial f}{\partial \sigma'^*_{ij}} C^e_{ijkl} \dot{\varepsilon}^*_{kl}}{\dfrac{\partial f}{\partial \sigma'^*_{mn}} C^e_{mnop} - \dfrac{\sqrt{3}}{3}\left(\dfrac{\partial f}{\partial \phi} \dfrac{d\phi}{d\varepsilon^p_{eq}} + \dfrac{\partial f}{\partial c} \dfrac{dc}{d\varepsilon^p_{eq}} \right)} \tag{2-28}$$

2.2 Hydraulic anisotropy

Darcy's law

The general Darcy flow law is used and defines the Darcy fluid velocity $\underline{q}_w$ as a linear function of permeability and the gradient of fluid pressure p_w :

$$\underline{q}_w = -\frac{\underline{\underline{K}}_w}{\rho_w . g}(\nabla p_w) = -\frac{\underline{\underline{k}}_{\text{int}}}{\mu_w}(\nabla p_w) \tag{2-29}$$

where $\underline{\underline{K}}_w$ is the anisotropic tensor of permeability. This tensor has nine components and may be written in a general form as follows:

$$\underline{\underline{K}}_w = \begin{bmatrix} K_{xx} & K_{xy} & K_{xz} \\ K_{yx} & K_{yy} & K_{yz} \\ K_{zx} & K_{zy} & K_{zz} \end{bmatrix}$$

$\underline{\underline{k}}_{\text{int}}$ is the intrinsic permeability [m²] and μ_w is the fluid dynamic viscosity [Pa/s].

$\underline{\underline{k}}$ depends on the degree of saturation of the material:

$$\underline{\underline{k}} = k_r \ \underline{\underline{k}}_{sat} \tag{2-30}$$

with k_r being the relative permeability coefficient defined by Marschall et al. (2005) for the Opalinus Clay as:

$$k_r = \sqrt{S_r}\left(1-(1-S_r{}^2)^{0.5}\right)^2 \tag{2-31}$$

where S_r is the degree of saturation.

Retention curve

The degree of saturation is related to suction by the following expression:

$$S_r = \left(1+\left(\frac{-p_w}{CSR1}\right)^{CSR2}\right)^{-\left(1-\frac{1}{CSR2}\right)} \tag{2-32}$$

where CSR1 and CSR2 are material parameters.

Water specific mass

The water specific mass depends on pore water pressure:

$$\rho_w = \rho_{w0}\left[1+\frac{p_w - p_{w0}}{\chi_w}\right] \tag{2-33}$$

where ρ_{w0} is the reference water specific mass at reference pore water pressure χ_w is the liquid compressibility coefficient.

2.3 Balance equations

Momentum balance equation

The momentum balance equation is written for quasi-static conditions:

$$div(\sigma_{ij}) = 0 \tag{2-34}$$

where σ_{ij} is the total stress tensor [Pa] expressed by:

$$\sigma_{ij} = \sigma'_{ij} - b\ S_r\ p_w \tag{2-35}$$

where b is the Biot coefficient and σ'_{ij} the effective stress.

Water mass balance equation

We suppose that the water is only in the liquid phase. Then, the water mass balance equation can be written:

$$\frac{\partial}{\partial t}\left(\rho_w n S_r\right) + div\left(\rho_w\ \underline{q}_w\right) = Q_w \tag{2-36}$$

where $\underline{q}_w$ is the mean speed of the liquid phase compared to the solid phase [m.s^{-1}] and ρ_w is the bulk density of water [kg.m^{-3}].

3 Model parameters identification

3.1 Mechanical parameter estimation from triaxial tests

Laloui and François (2008) have compiled triaxial tests results corresponding to three different inclinations of the bedding plane with respect to the loading direction σ_1 (Figure 7):

- Loading parallel to bedding planes: P-Sample, α_{σ_1} = 90°
- Loading perpendicular to bedding planes: S-Sample, α_{σ_1} = 0°
- Loading with an inclination of 45° to bedding planes: Z-Sample, α_{σ_1} = 45°

These triaxial tests have been performed under 4 different confinement pressures σ_3 equal to: 0, 5, 10 and 15MPa (Figure 8). The geomechanical characteristics have been determined through the comparison between these experimental results and their simulations based on the Drucker-Prager elastoplastic model without hardening/softening regimes.

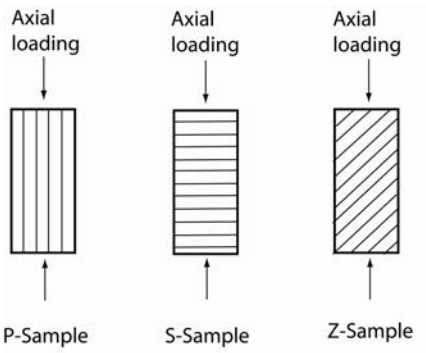

Figure 7: Orientation of bedding with respect to the loading direction in P-, S- and Z- samples

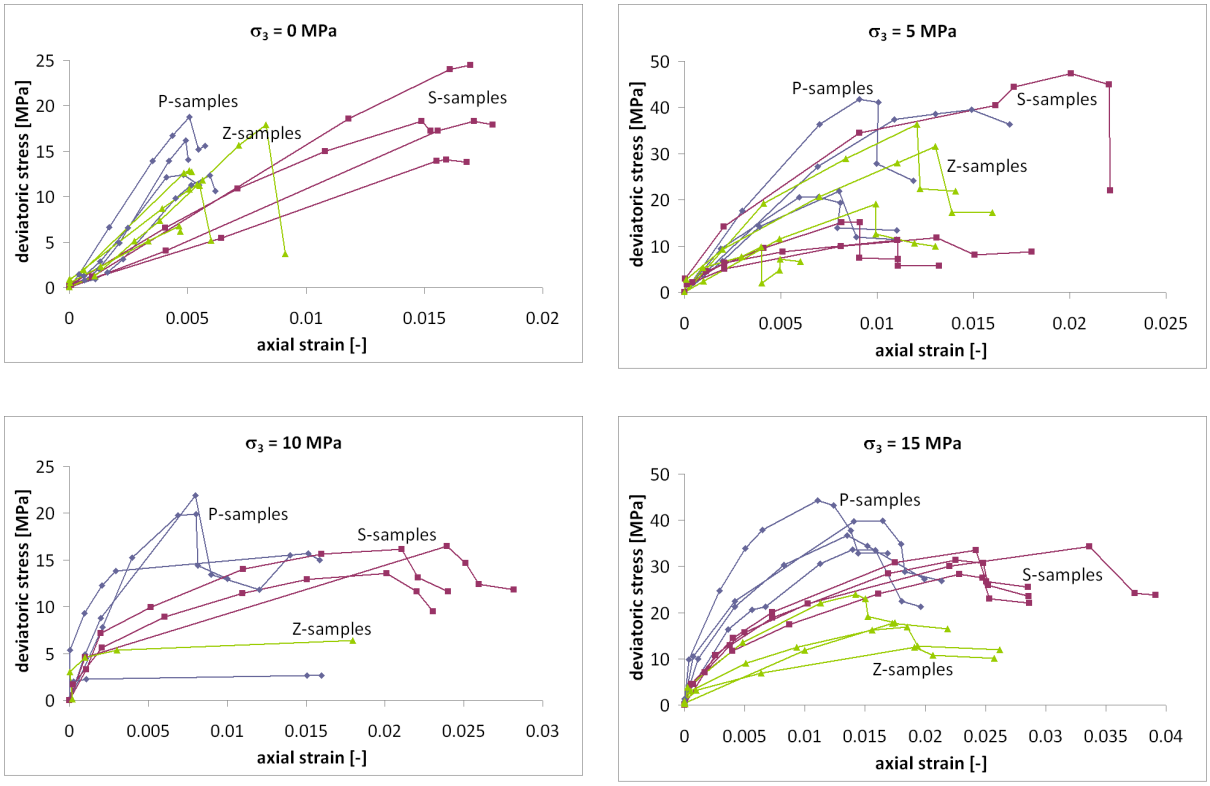

Figure 8: Triaxial results under 4 different confinement pressures σ_3 for three different inclinations of the bedding plane with respect to the loading direction σ_1

Plastic parameter calibration

Assuming that plastic anisotropy only concerns cohesion parameter and not friction angle, the same friction angle $\varnothing_c$ has been considered in all directions (as commonly admitted in literature – cf. Bock 2001) and fixed to 20°. Cohesions are estimated from (p,q) graph drawn for each case (Figure 9). According to failure criteria given in equations (2-12) and (2-16) without taking into account hardening parameters in the behaviour, we obtain by considering only the most relevant ($p,q_{failure}$) points:

$$c_{0°} = 6.4\text{MPa}, \qquad c_{45°} = 1.8\text{MPa}, \qquad c_{90°} = 4.5\text{MPa}.$$

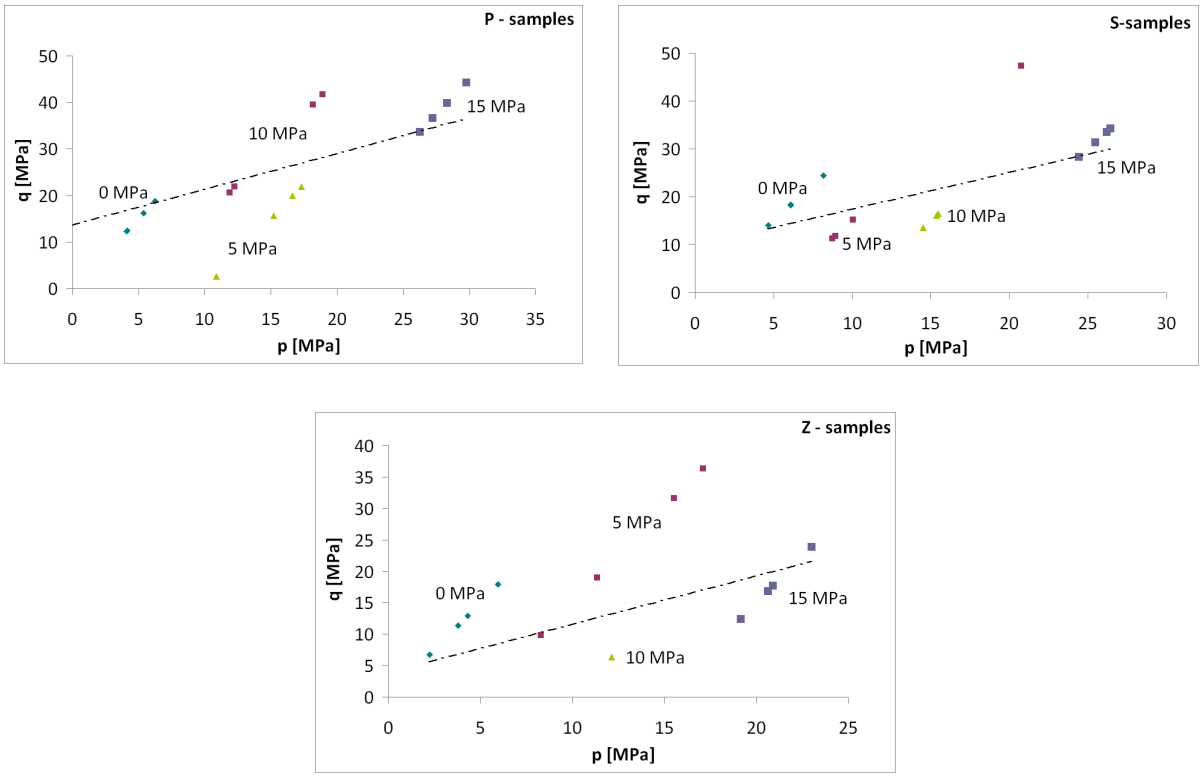

Figure 9: Failure criteria in (p, q) plane for three different inclinations of the bedding plane with respect to the loading direction σ_1

Elastic parameter calibration

Identification of Poisson's ratio can not be easily performed on triaxial test results. Its value with bedding orientation is chosen according to literature (Gens et al. 2007, Wileveau 2005, Martin and Lanyon 2003, Bock 2001):

$$\upsilon_{//\,//} = 0.33 \qquad \upsilon_{//\perp} = 0.24$$

Young's modulus is identified on all triaxial tests. By averaging estimation for each loading case, we obtain the values summarized in Table 1 associated to numerical modelling results presented in Figure 10. They show that the elastic stiffness's (and the corresponding shear strengths) are clearly affected by initial stress state as well as the direction of loading with respect to the bedding plane.

Table 1: Young modulus identification on triaxial test with bedding orientation

σ_3 [MPa]	$E_{//}$ [GPa] P-samples	$E_{\perp}$ [GPa] S-samples	$E_{45°}$ [GPa] Z-samples
0	3.2	2.2	2.3
5	4.6	3.5	3.2
10	5.9	4.9	4.1
15	7.2	6.2	4.0

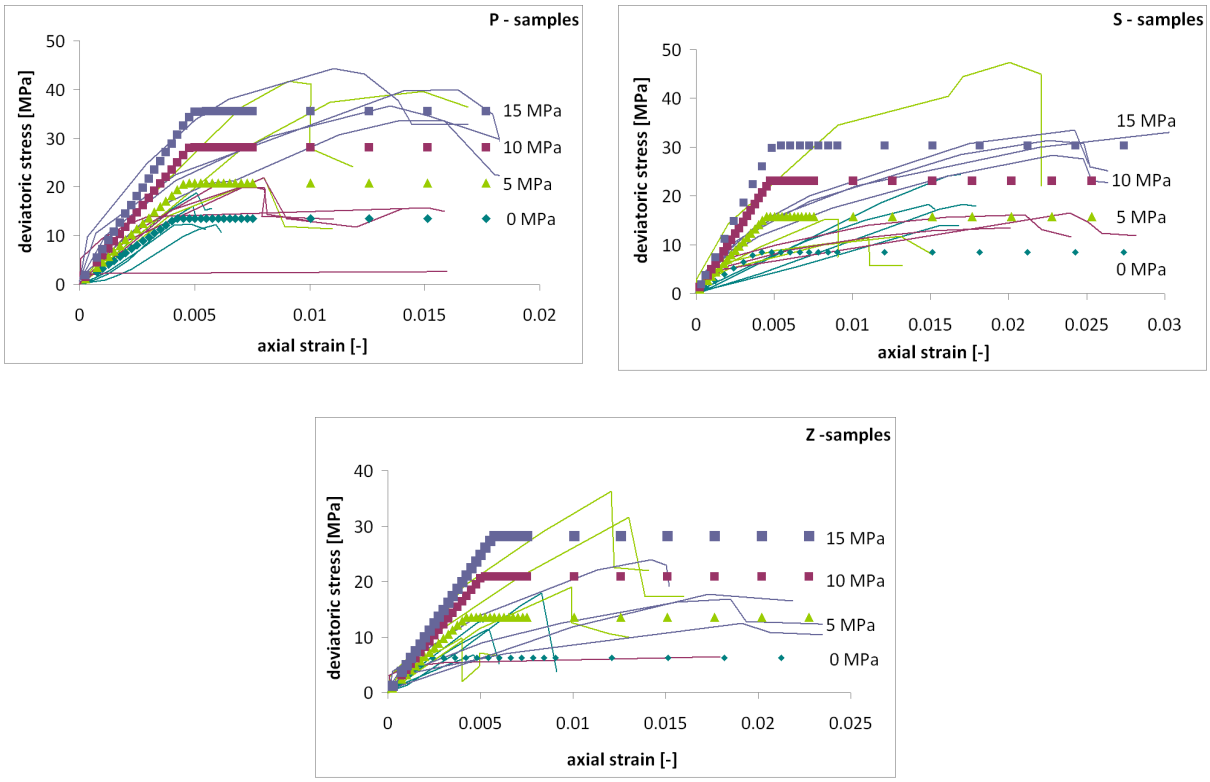

Figure 10: Triaxial tests calibrations under 4 different confinement pressures σ_3 for three different inclinations of the bedding plane with respect to the loading direction σ_1

3.2 Hydraulic parameters

The hydraulic parameters presented in Table 2 have been obtained from the literature (Gens et al. 2007, Wileveau 2005, Martin and Lanyon 2003).

Table 2: Hydraulic characteristics

Initial porosity	[-]	n_0	0.1
Initial intrinsic permeability	[m²]	$k_{sat,//}$	2.10^{-20}
		$k_{sat,\perp}$	8.10^{-21}
Water specific mass	[kg/m³]	ρ_w	1000
Fluid dynamic viscosity	[Pa.s]	μ_w	10^{-3}
Liquid compressibility coefficient	[MPa^{-1}]	$1/\chi_w$	5.10^{-4}
Coefficient of the water retention curve	[MPa]	CSR1	5
	[-]	CSR2	1.2

4 2D Modelling of tunnel excavation

Based on the in-situ measurements, the objective of the modelling of the excavation phase is to identify the concepts, the processes and the parameters of models in order to reproduce the creation and evolution of the EDZ. Also, these modelling will indicate the accuracy and the relevance of current models to predict EDZ structure.

4.1 Geometry, boundary conditions and loading description

The HGA microtunnel has been excavated from a niche of the Gallery 04 of the Mont-Terri Underground Research Laboratory (URL). The drilling is parallel to the bedding orientation. In a section perpendicular to the microtunnel, the bedding plane is oriented at 45° with respect to horizontal direction (Figure 11).

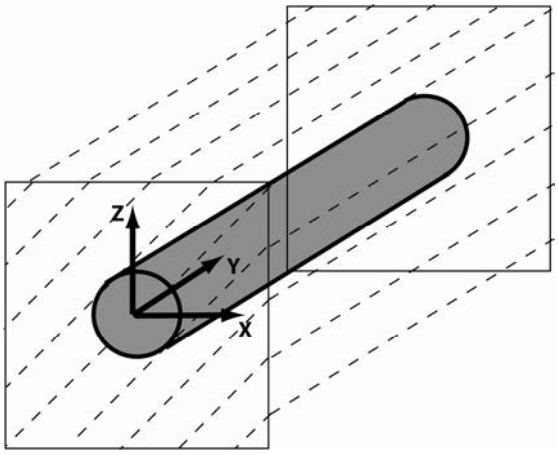

Figure 11: Schematic view of the orientation of the HGA gallery with respect to bedding plane.

The problem has been considered as a 2D plane strain problem, considering a perpendicular section in the middle of the gallery. A 40m wide square domain has been considered. The initial stress is anisotropic:

- σ_Z = 6.5MPa (vertical stress),
- σ_X = 4.4MPa (horizontal radial stress)
- σ_Y = 2.2MPa (horizontal axial stress)

The initial pore water pressure has been fixed to 0.9MPa. Because of the bedding anisotropy and the initial stress state does not follow the same orientation planes, the whole cross section needs to be taken into account in our model (no symmetry exists, see Figure 12).

In term of mechanical conditions, the external boundaries are kinematically constrained (no displacement). The internal boundary (at the microtunnel wall) is stress controlled. To simulate the excavation phase, the total stress at the microtunnel wall is decreased from the initial anisotropic stress to 0MPa within 7 day. The pore water pressure is maintained constant at 0.9MPa on the external boundaries while the pore water pressure at the microtunnel wall is reduced from 0.9MPa to 0.1MPa in 7 day (see Figure 13).

Afterward, a ventilation is put in place with a relative humidity RH = 83% and a temperature T = 13°C in average. To reproduce microtunnel ventilation, pore water pressure is linearly

decreased from 0.1 to a given suction in 7 days and then a constant pressure is maintained. Suction can be estimated as follow:

$$P_w - P_a = \frac{\rho_w RT}{M_w} \ln(RH) = -23.9MPa \tag{4-1}$$

The hydro-mechanical response of Opalinus Clay around the excavated microtunnel has been simulated over a period of 322 days (from 18th February to 31st December 2005). The numerical results are compared with in-situ measurements in sensor HG-A2 and HG-A3 for pore water pressure and HG-A5 and HG-A7 for displacements. The locations of the sensors projected on one plane perpendicular to HGA borehole are reported in Figure 14. Some pore water pressure and displacement evolutions with time measured in situ are drawn in Figure 15.

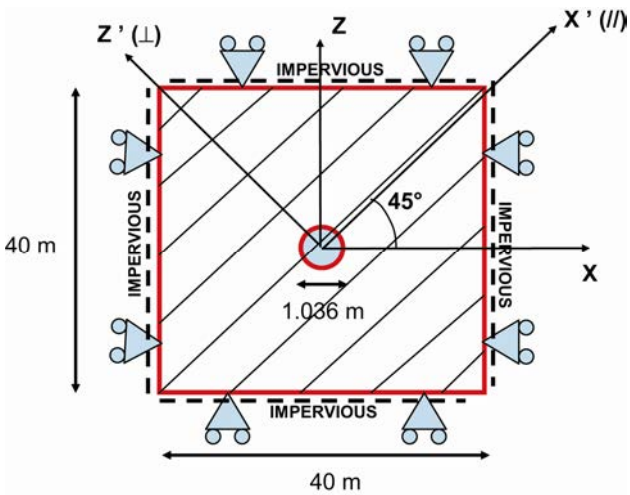

Figure 12: Boundary conditions of the 2D plane strain model.

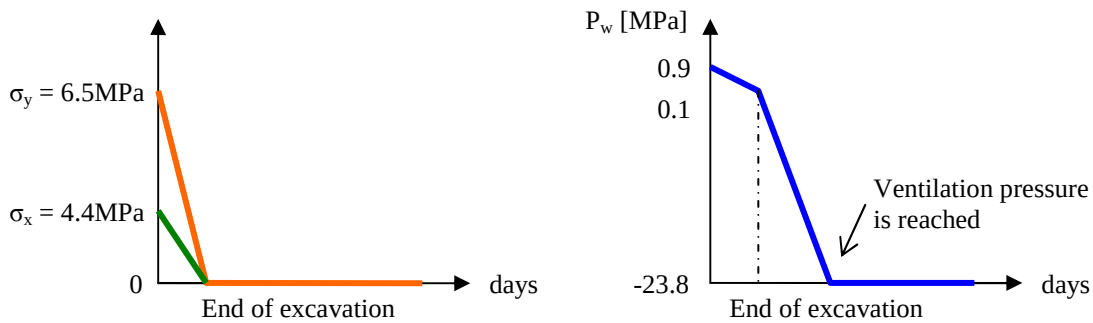

Figure 13: Hydromechanical loading (subtask 1)

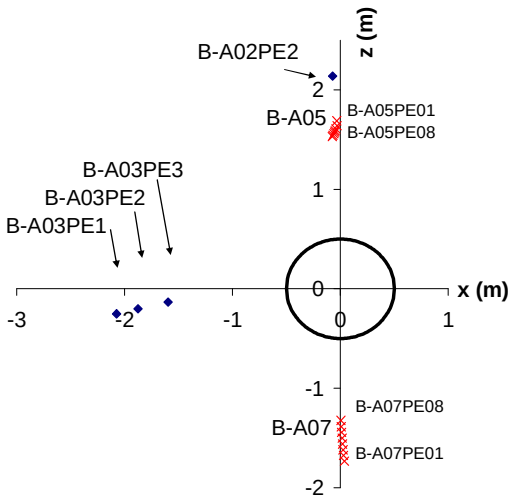

Figure 14: Projection of the sensor location in the 2D modelling section.

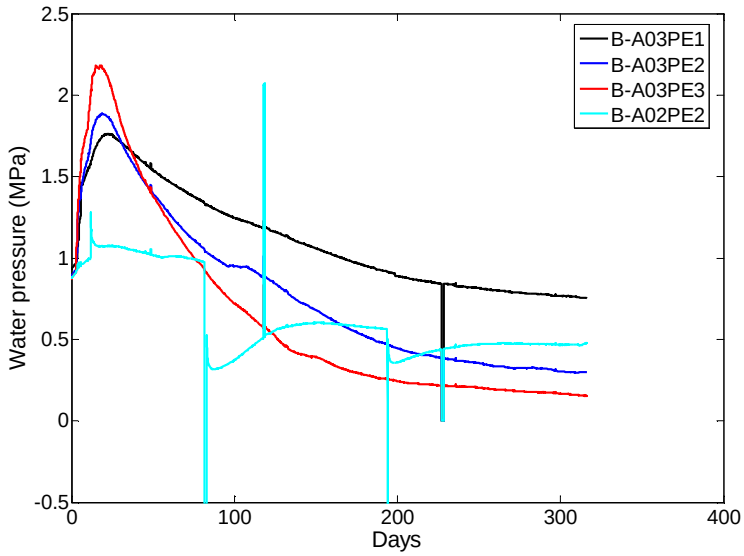

(a) Experimental results of the time evolution of the pore water pressure in sensor HG-A02 and HG-A03

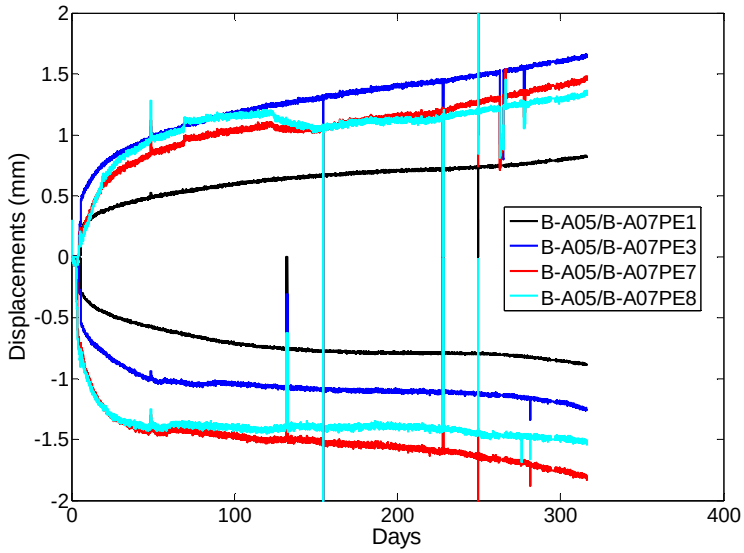

(b) Experimental results of the time evolution of the total displacement in sensor HG-A05 and HG-A07

Figure 15: Experimental measurements around HGA tunnel

4.2 Hydromechanical parameters

The parameters initially consider in the Drucker-Prager elastoplastic model corresponds to the values identified on triaxial tests and summarized in Table 1 (for mechanical properties) and in Table 2 (for hydraulic properties). In this model, no hardening neither softening is included, which means that cohesion and friction angle do not evolve. No dilatancy is also taken into account. Furthermore, the model does not consider any evolution of Young's modulus with stress state. Only one single value of E is included in each direction of anisotropy. By considering as initial stress the horizontal value $\sigma_X = \sigma_3 = 4.4$MPa, the anisotropic values of E have been evaluated by linear interpolations of Table 1 estimations. Then, it follows: $E_{//} = 4.4$GPa and $E_{\perp} = 3.3$GPa. All the useful parameters are summarized in Table 3.

Table 3: Opalinus Clay parameters

Physical parameters			
Initial porosity	[-]	n_0	0.1
Volumic mass	[kg/m³]	ρ	2450
Water specific mass	[kg/m³]	ρ_w	1000
Water content	[%]	W	6.1
Fluid dynamic viscosity	[Pa.s]	μ_w	10^{-3}
Liquid compressibility coefficient	[MPa^{-1}]	$1/\chi_w$	5.10^{-4}
Mechanical parameters			
Young's modulus	[GPa]	$E_{//}$	4.4
		$E_{\perp}$	3.3
Poisson's ratio	[-]	$\upsilon_{////}$	0.33
		$\upsilon_{//\perp}$	0.24
Shear modulus	[GPa]	$G_{////}$	1.6
		$G_{//\perp}$	1.3
Friction angle	[°]	$\varnothing_c$	20
Cohesion	[MPa]	$c_{0°}$	6.4
		$c_{45°}$	1.8
		$c_{90°}$	4.5
Dilatancy	[°]	ψ	0
Biot coefficient	[-]	b	0.6
Hydraulic parameters			
Initial intrinsic permeability	[m²]	$k_{sat,//}$	2.10^{-20}
		$k_{sat,\perp}$	8.10^{-21}
Coefficients of the water retention curve	[MPa]	CSR1	5
	[-]	CSR2	1.2

4.3 Qualitative analysis of numerical results

4.3.1 Influence of anisotropic settings on global behaviour

In this qualitative analysis, each kind of anisotropy is studied independently. Analysis of the effects of initial stress anisotropy, of Young's modulus anisotropy, of cohesion anisotropy and of the combined effects of these three kinds of anisotropy on stresses and on plastic indicator is first proposed on a purely mechanical model of tunnel excavation (meaning that hydraulic variables are fixed) and on coupled hydro-mechanical modelling. Then, analysis is extended to the effects of permeability anisotropy on coupled hydro-mechanical modelling.

Effect of initial stress anisotropy

In purely mechanical modelling, mechanical parameters are assumed isotropic. For each parameter, anisotropic values of Table 3 are averaged to give isotropic values. Then, Young's modulus E and Poisson's ratio υ are fixed respectively to 3.86GPa and 0.28. Anisotropy only comes from initial stress conditions: σ_Z = 6.5MPa (vertical stress), σ_X = 4.4MPa (horizontal stress). Tunnel excavation in these conditions provides an oval shape of tunnel due to stress redistribution corresponding to compression zone on horizontal axis and extension zone on vertical axis (Figure 16). As the vertical initial stress is higher than the horizontal one, plastic indicator describes an elliptic zone around tunnel for which the main orientation is horizontal. This plastic indicator is a reduced deviator equal to 1 if the current state is elasto-plastic (on the yield limit) and less than 1 otherwise (elastic behaviour). Maximal values reached are 0.817 horizontally and 0.257 vertically meaning that no plasticity is developed under this initial stress state.

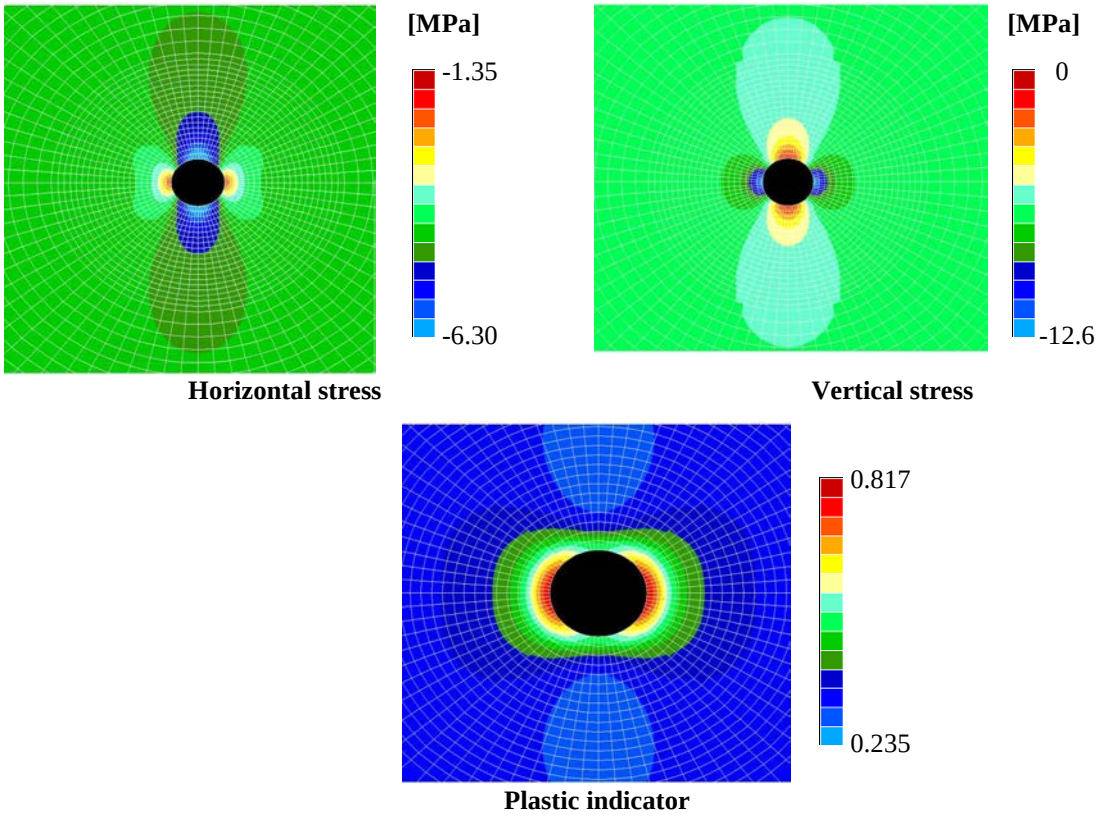

Figure 16: Effect of initial stress anisotropy on horizontal and vertical stresses and plastic indicator in purely mechanical modelling at the end of excavation phase

In coupled hydro-mechanical modelling, the same mechanical parameter than previously are considered. For hydraulic parameters, permeability is assumed isotropic and fixed to k = $1.4.10^{-20}$m². In these conditions, plastic indicator field follows the same shape around tunnel after excavation than in purely mechanical modelling but the maximal values reached are slightly higher (PI_{max} = 0.846). Furthermore, high overpressures of water are observed horizontally around tunnel. Vertically, pore water pressures are smaller than the initial ones as shown in Figure 17. These perturbations in pore water pressure field are the results of stress concentrations around tunnel due to excavation.

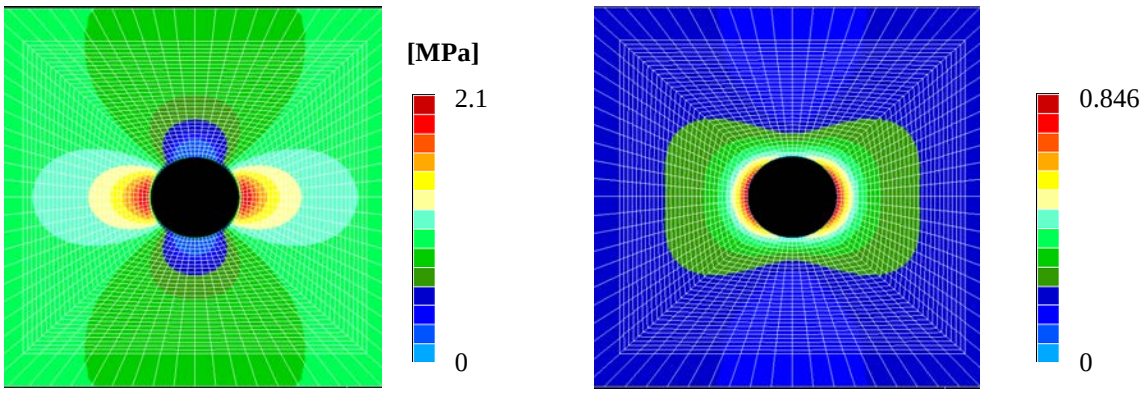

Water pressure **Plastic indicator**

Figure 17: Effect of initial stress anisotropy on water pressure and plastic indicator in coupled hydro-mechanical modelling at the end of excavation phase

Effect of mechanical parameter anisotropy

Young modulus anisotropy

In this purely mechanical modelling, initial stresses and Poisson's ratio are assumed isotropic, and fixed to $\sigma_Z = \sigma_X$ = 4.4MPa and υ = 0.28. Anisotropy only comes from Young modulus: $E_{//}$ = 4.4GPa and $E_{\perp}$ = 3.3GPa, oriented at 45° (along bedding plane). Tunnel excavation in these conditions provides slight oval shape of tunnel oriented at 45°, which is not sufficient to generate significant changes in stress redistributions. Stresses and plastic indicator are quite similar to cases without any anisotropy (Figure 18, plastic indicator is limited to 0.494).

Cohesion anisotropy

Adding plastic anisotropy, through cohesion: $c_{0°}$ = 6.4MPa, $c_{45°}$ =1.8MPa and $c_{90°}$ = 4.5MPa, provides no more plasticity during excavation in purely mechanical modelling. Stress redistribution around tunnel is similar to the previous case. Plastic indicator value is less than 1, but its distribution follows new orientations: maximal values are oriented along directions at 0° and 90°, minimal values are oriented along directions at ±45° (Figure 19).

However, in coupled hydro-mechanical modelling (in which permeability is assumed isotropic and fixed to k = $1.4.10^{-20}$m²), stress concentration increases and plasticity is developed in directions along which principal stress is oriented at 45° with bedding (Figure 20). In fact, high overpressures of water are observed along bedding. They influence plastic indicator field that follows the same shape around tunnel than in purely mechanical modelling but now PI_{max} = 1 is reached.

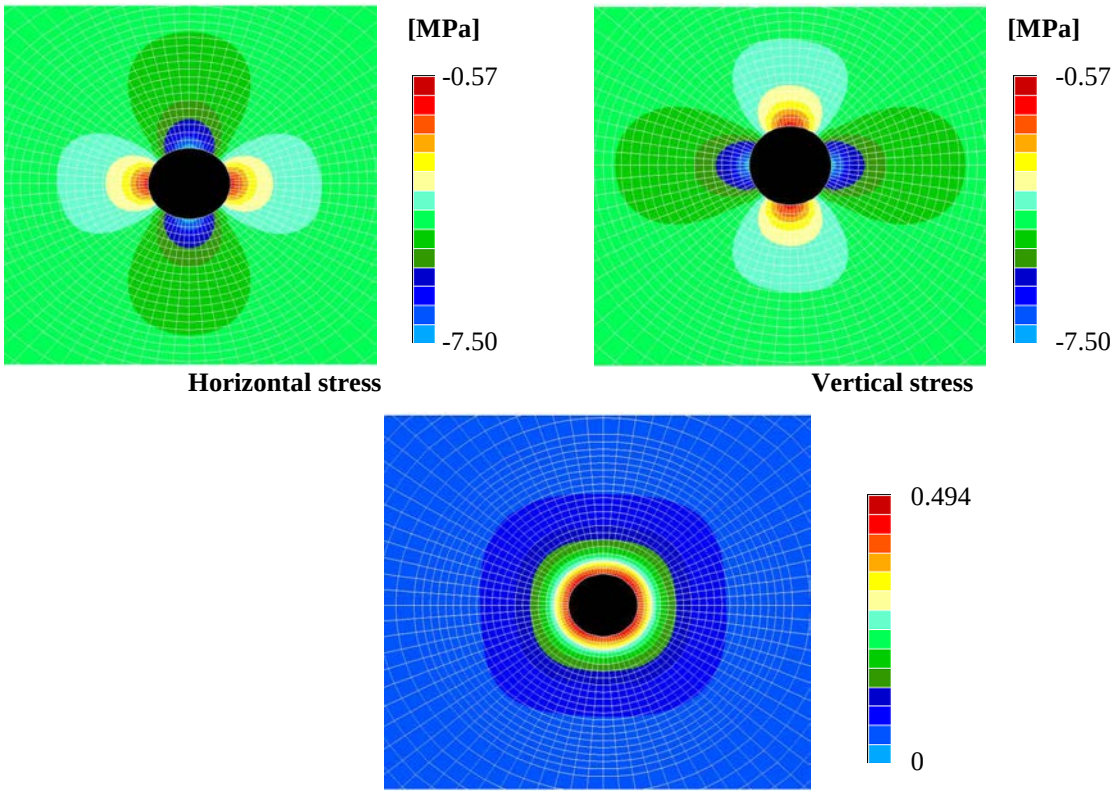

Figure 18: Effect of Young modulus anisotropy on horizontal and vertical stresses and plastic indicator in purely mechanical modelling at the end of excavation phase

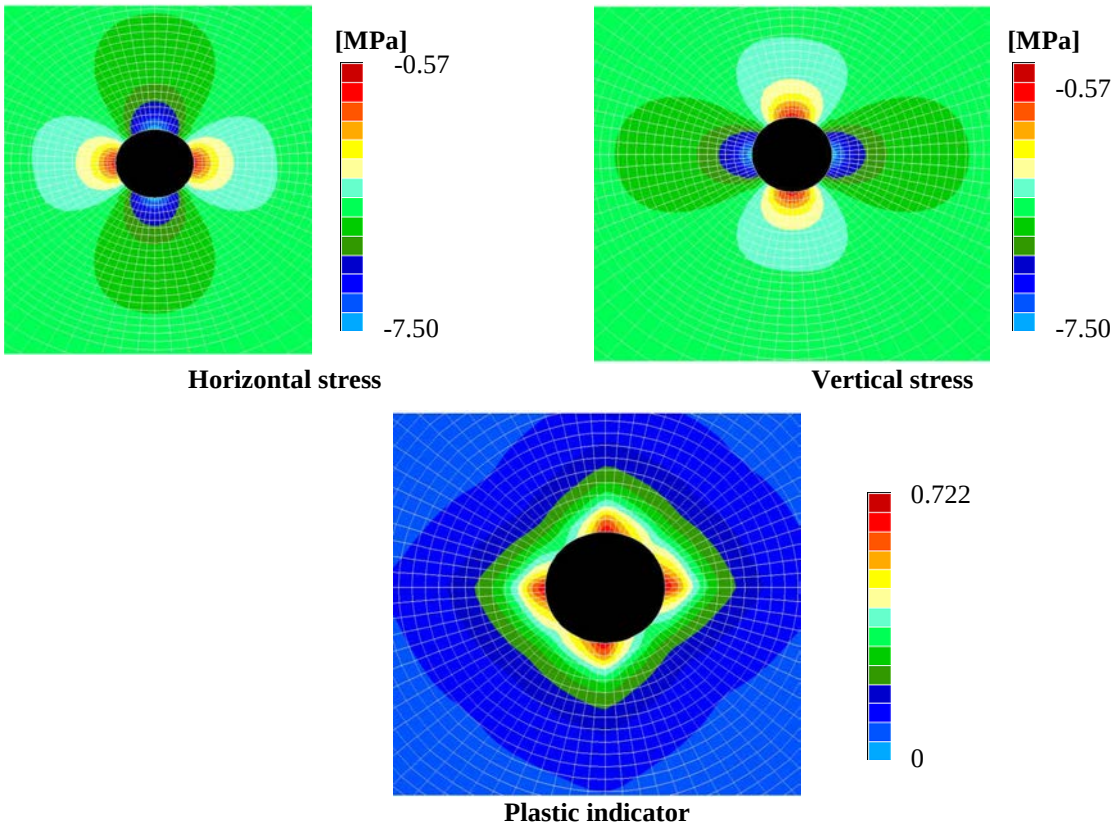

Figure 19: Effect of cohesion anisotropy on horizontal and vertical stresses and plastic indicator in purely mechanical modelling at the end of excavation phase

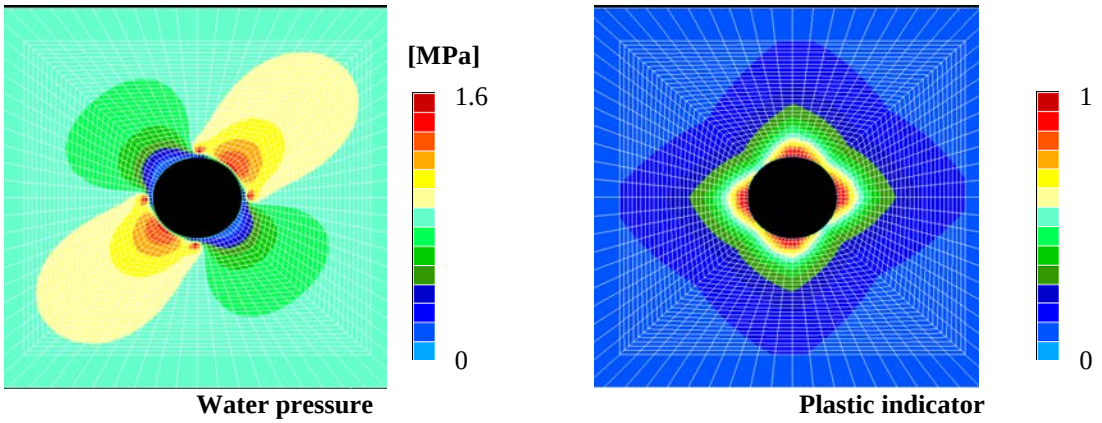

Figure 20: Effect of cohesion anisotropy on water pressure and plastic indicator in coupled hydro-mechanical modelling at the end of excavation phase

Combined effects of initial stress and mechanical anisotropies

If the three previous sources of anisotropy are considered simultaneously on purely mechanical modelling, tunnel excavation provides an oval shape of tunnel oriented at +11° with the horizontal direction. However, after the excavation phase, stress redistribution directions are closed the horizontal one like in the case where initial stresses anisotropy is only considered. Effects of elasto-plastic anisotropy are too small to be significant on orientations; only a slight rotation can be noticed (Figure 21). However, elasto-plastic anisotropy influences the level of stress reached around excavation by intensifying the horizontal compression zone and the vertical extension zone. In term of plastic indicator, maximum value is reached and equal to 1 near the horizontal direction. It means that only the coupling between anisotropies of initial stresses, elastic and plastic parameters can provide plasticity in the purely mechanical model.

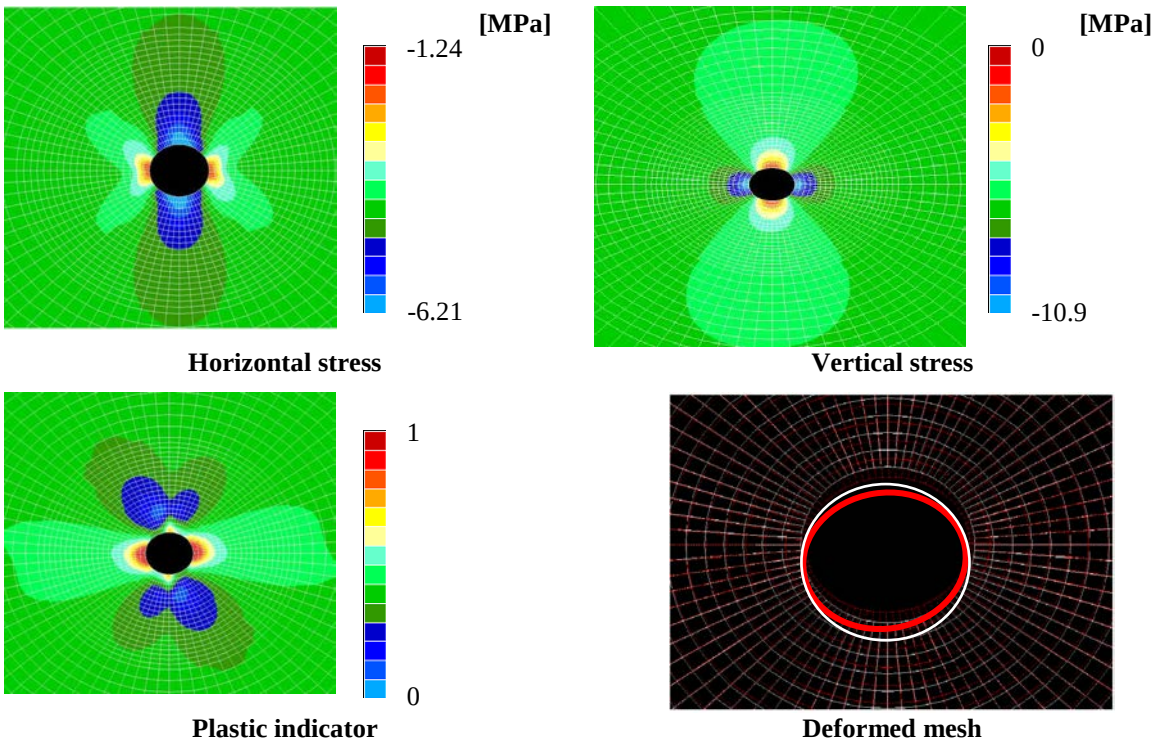

Figure 21: Simultaneous effect of initial stress, Young modulus and cohesion anisotropies on horizontal and vertical stresses, plastic indicator and deformed mesh in purely mechanical modelling at the end of excavation phase

By considering coupled hydro-mechanical modelling (in which permeability is assumed isotropic and fixed to $1.4.10^{-20}m^2$), both excavation and ventilation of the HGA borehole can be modelled and compared. As described in section 4.1 and Figure 13, excavation modelling is performed in 7 days and is followed by ventilation phase. During 1 week, capillary pressure is reduced to reach -23.8MPa. Finally, pressure is kept constant for 10 months.

At the end of excavation phase: the presence of water generates a decrease of effective stresses and plastic criteria compare to previous cases, extending a little bit the plastic zone (Figure 22). On water pressure distribution, two zones with very high pressures can be distinguished in a direction close to the horizontal one. Notice that the observed slight rotation of these zones in comparison to Figure 17 is the result of coupling with mechanical parameter anisotropy (Figure 20). In extension area, porosity increases and water pressure decreases because of mechanical anisotropy. It results a diminution of saturation degree and suction.

After 10 months of ventilation at 83% of relative humidity creates suction of -23.9MPa on the tunnel wall and the diminution of saturation degree. It provides an increase of effective stress all around the tunnel borehole. It is followed by a decrease of plastic indicator for which the maximal value is now equals to 0.773, meaning that no more plasticity is developed.

After excavation:

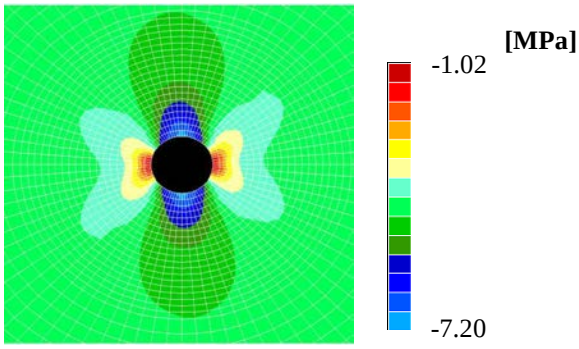

Horizontal stress

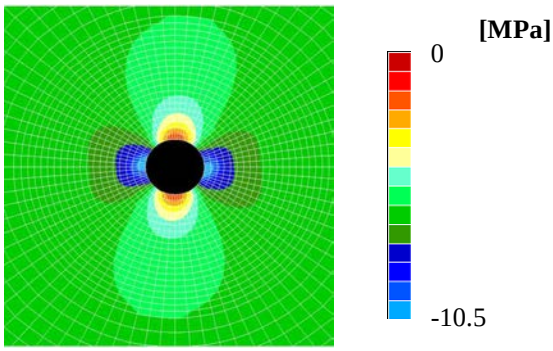

Vertical stress

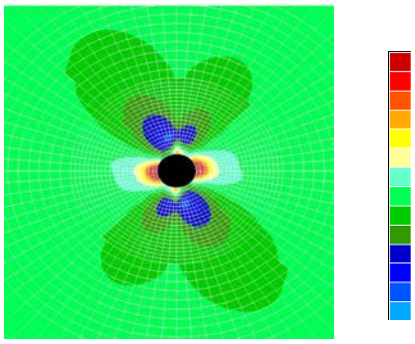

Plastic indicator

After 10 months of ventilation:

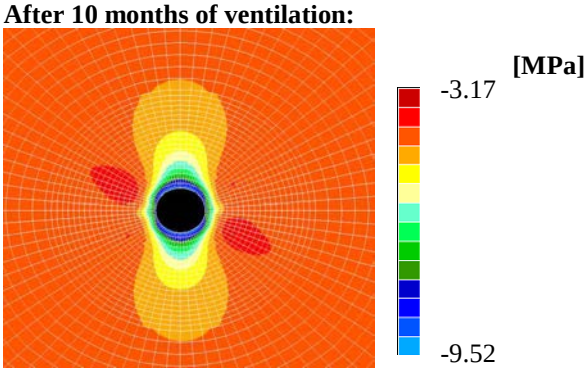

Horizontal stress

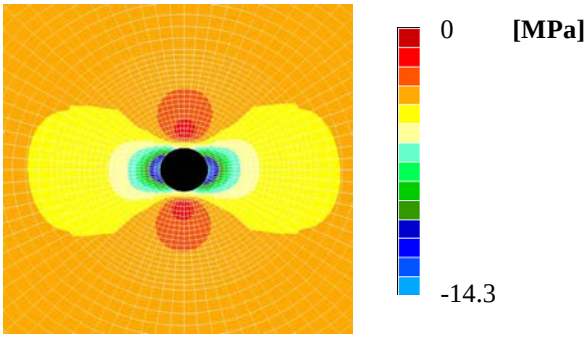

Vertical stress

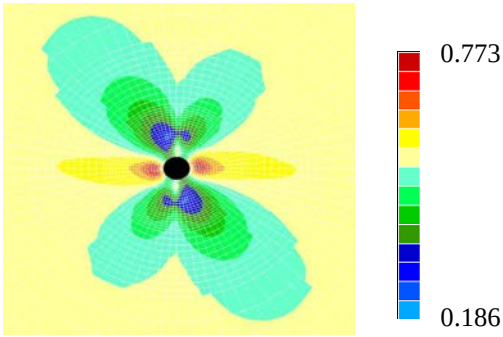

Plastic indicator

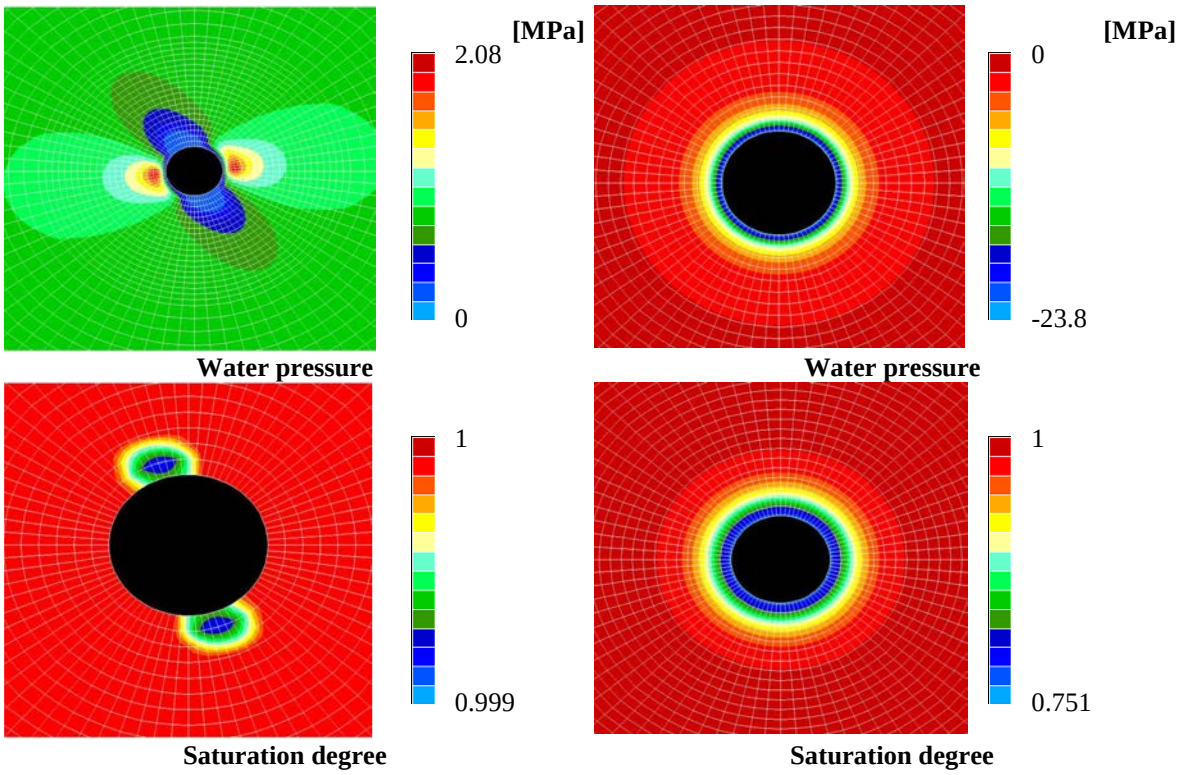

Figure 22: Simultaneous effect of mechanical anisotropies on hydro-mechanical modelling with isotropic hydraulic conditions at the end of excavation phase and after 10 months of ventilation

Effect of permeability anisotropy

In previous calculations, anisotropy of permeability is not considered in hydraulic conditions. Here, excavation of the HGA borehole is modelled in order to put in evidence the effect of permeability and its anisotropy on hydro-mechanical modelling. Then, initial stresses, Young modulus and Poisson's ratio are assumed isotropic, meaning that $\sigma_Z = \sigma_X = 4.4$MPa, Young's modulus E and Poisson's ratio υ are fixed respectively to 3.86GPa and 0.28. Anisotropy comes from permeability: $k_{//} = 2.10^{-20}$m² and $k_{\perp} = 8.10^{-21}$m² (i.e. anisotropy of permeability is characterized by a higher value in a direction parallel to bedding than in a normal direction). Contrary to what could be expected, anisotropy of permeability has a weak influence on pore water pressure field. Water overpressures are concentrated on a small ring around tunnel, modifying slightly plasticity index field obtained without any anisotropy (PI_{max} = 0.752 - Figure 23).

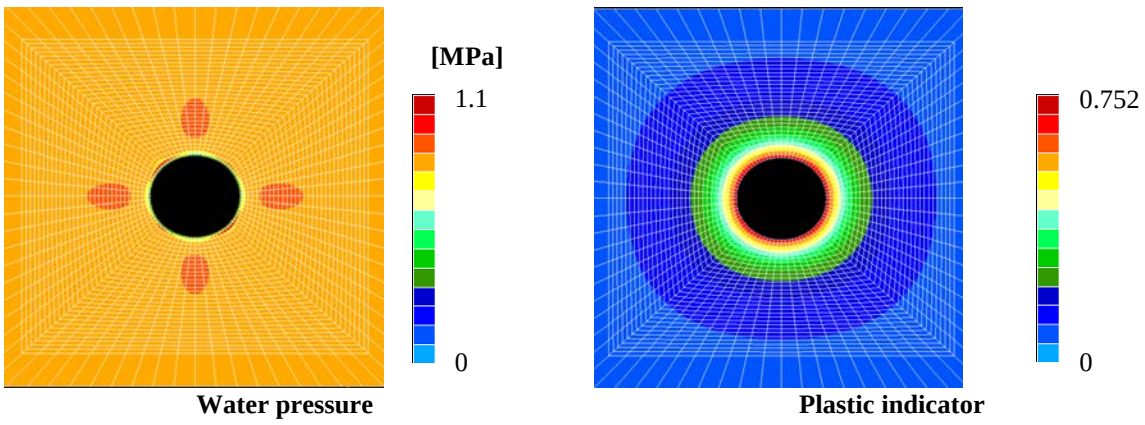

Figure 23: Effect of permeability anisotropy on water pressure and plastic indicator in coupled hydro-mechanical modelling at the end of excavation phase

Combined effects of all anisotropy sources

Finally, all the anisotropic properties of the Opalinus Clay behaviour in HGA problem are considered: initial stresses, Young's modulus, cohesion and permeability. Results are summarized in Figure 24.

After excavation, permeability anisotropy is too small to be observed on stress field as well as water pressure and saturation degree. However, it has stronger effects on pore pressure during and after ventilation. After excavation, two overpressure areas are noticed closed to horizontal directions. These overpressures still increase during the week before capillary pressure reaches -23.8MPa. They are drained only since ventilation is keeping constant. Then, the anisotropy of permeability provides a stronger desaturation in a direction parallel to the bedding. Water pressure field around tunnel is inclined in an average direction due to coupling between anisotropy sources, modifying stress field and plastic indicator shape. Deformed mesh of tunnel excavation is oriented at +13° with the horizontal direction just after excavation. After 10 months of ventilation, inclination increases of 4°. Notice that all these phenomena are limited due to a small permeability anisotropy ratio: $k_{//} / k_{\perp} = 2.5$. In the case of this ratio is exaggerated ($k_{//} / k_{\perp} = 2.5\ 10^5$ for instance), water overpressures are reduced after the ventilation phase and oriented along bedding plane after excavation as shown in Figure 25.

After excavation:

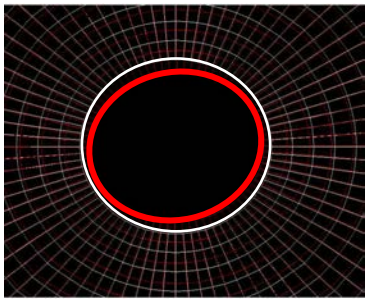

Deformed mesh

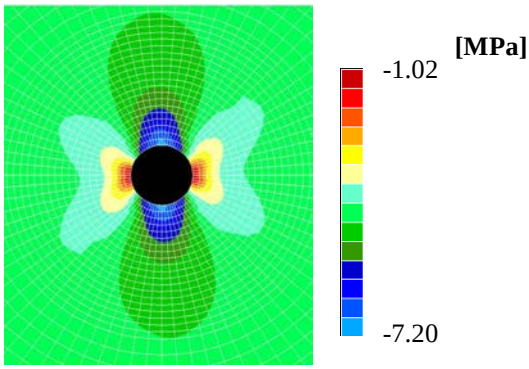

Horizontal stress

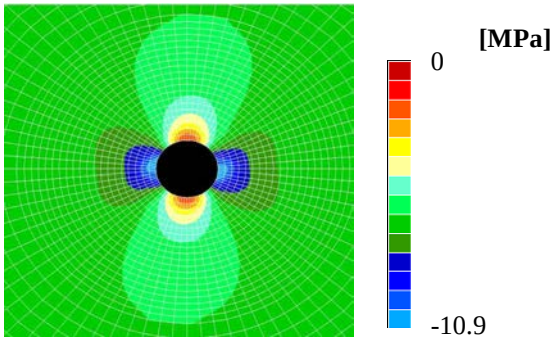

Vertical stress

After 10 months of ventilation:

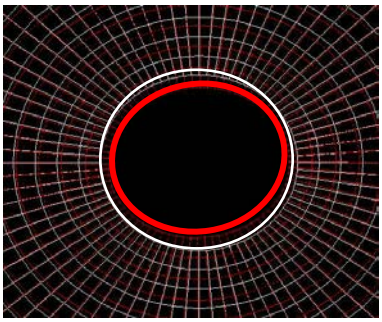

Deformed mesh

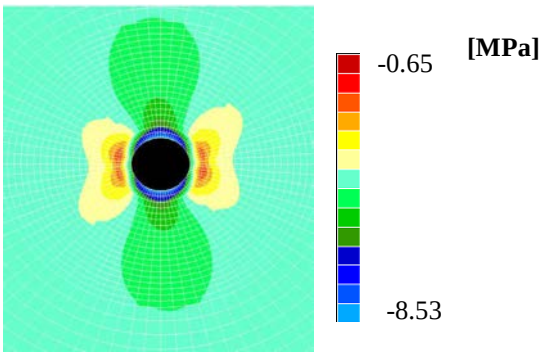

Horizontal stress

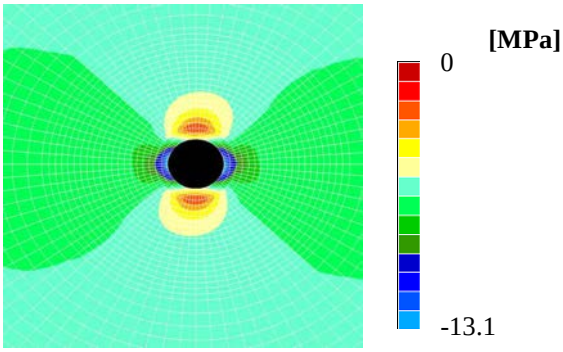

Vertical stress

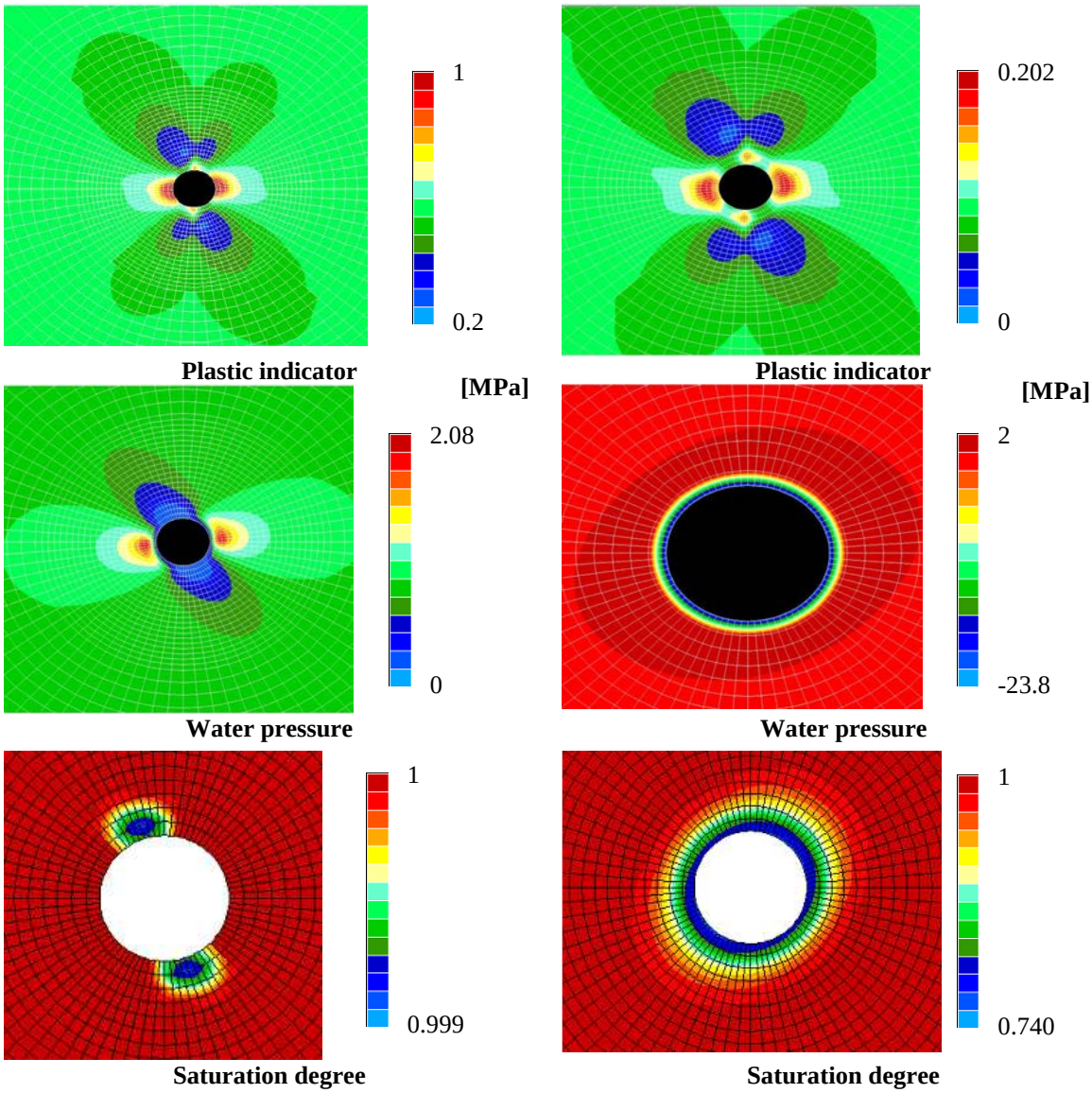

Figure 24: Simultaneous effect of mechanical anisotropies on hydro-mechanical modelling with anisotropic hydraulic conditions at the end of excavation phase and after 10 months of ventilation

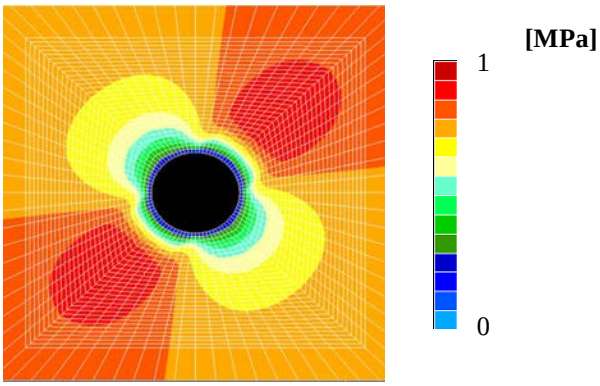

Figure 25: Simultaneous effect of mechanical anisotropies on water pressure field with anisotropic hydraulic conditions and exaggerated permeability anisotropic ratio after 10 months of ventilation

4.3.2 Interpretation of numerical results

Because of the difference sources of anisotropy, the hydro-mechanical response of Opalinus Clay around the excavated gallery is not axisymmetric. The anisotropic stress state tends to induce two distinct behaviours on vertical and horizontal directions: an extensional behaviour (negative variation of pore water pressure) in the vertical direction and a compressive behaviour (positive variation of pore water pressure) in the horizontal direction (Figure 16). On the contrary, elastic anisotropy provides higher variation of pore pressure in the stiffer direction (parallel to bedding) and less variation of pore pressure (or even negative variation) in the less rigid direction (perpendicular to bedding – Figure 22). Finally, anisotropic permeability makes drainage faster in the direction parallel to bedding (Figure 24). So, the combination of all sources of anisotropy makes complex the pore water pressure evolution.

Figure 24 shows the pore water pressure distribution immediately after excavation and after 10 months of ventilation, respectively. After ventilation of the gallery, the negative pore water pressure propagates faster in the most permeable direction (parallel to bedding). The deformed mesh one year after the excavation presents minimum and maximum displacements occurring at 9° and 99° with respect to x axis, respectively. It corresponds to preferential directions in which plastic zone develops after excavation. Those directions correspond to the zone in which maximum shear stresses are concentrated. At the end of the simulation, the negative pore water pressure (suction) induced by the gallery ventilation provokes an increase in strength. It results that the plastic processes disappear and the behaviour is elastic.

Comparison with in situ observed phenomena

These previous numerical results can be compared to in situ observed phenomena. Figure 26 presents a picture of HGA borehole and its interpretation in term of damage. Two different damages can be distinguished:

- First, damage zones referred as “b” are slightly inclined to horizontal axis. They correspond to stress concentration providing plasticity and large water pressure evolution after excavation as shown in Figure 24 or Figure 21.
- Second, damage zones referred as “a” correspond to excavation shell at around 45°, parallel to bedding, where water pressure and saturation degree decrease after excavation and where the gradient of saturation degree strongly decreases during the ventilation phase (see Figure 24). Stress modifications in this direction could also reactivate bedding planes and generate some additional failures. Then, the “a”-zones may be viewed as an excavation damaged zones due to hydraulic anisotropy effects during ventilation. One can remark that failure impact zone seems to be larger in the top than in the bottom on Figure 26 because of tectonic fault planes weakening the rock in a direction subparallel to bedding (as demonstrated in the following, see section 4.4.3).

Qualitatively, numerical results seem realistic and reliable to interpret observed phenomena. However quantitatively, comparison between experimental measurements and numerical results of water pressure evolution in the lateral HG-A3 borehole (Figure 27) shows that modelling is not sufficient to reproduce phenomena. Numerical simulation is able to reproduce the main trends of pore water pressure evolutions but some discrepancies between numerical and experimental results still exist. For instance, we can notice that:

- the intensity of the peak of the pore water pressure evolution measured by sensor HG-A3 is underestimated by the numerical simulations;

- the pore water pressure increase before the peak is not delayed at the beginning of ventilation phase;
- the pore water pressure decreases faster after the peak in the numerical simulations than observed in situ.

It means that some complementary investigations are necessary to improve the 2D plane strain analysis as proposed in the following.

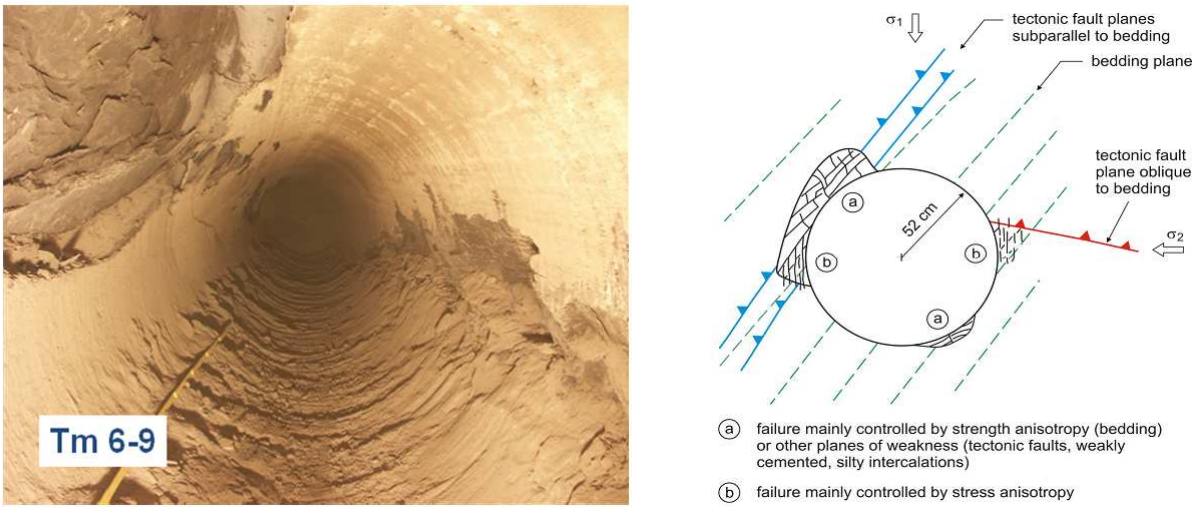

(a) **(b)**

Figure 26: (a) Picture of HGA borehole; (b) Schematic view of damage

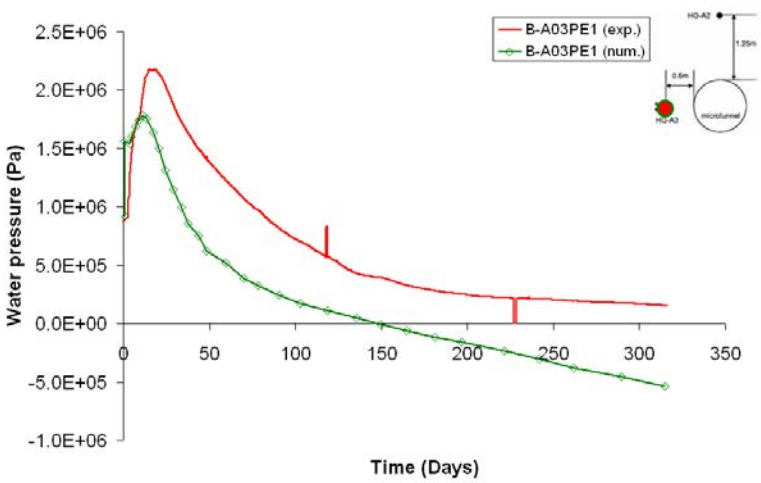

Figure 27: Water pressure evolution with time in HG-A3 borehole – first comparison between experimental measurements and numerical results

4.4 Complementary investigations for quantitative analysis

In order to improve the 2D plane strain numerical analysis of HGA microtunnel excavation, some complementary investigations are proposed based on the influences of mesh size, the presence of the main gallery and of a tectonic fault or the creation of an Excavation Damaged Zone around boreohle.

4.4.1 Mesh sensitivity around HGA borehole

In the finite element analysis, some overpressures can not correspond to any physical effects but may be the consequences of numerical instabilities, like oscillations, due to un-adapted mesh. As we have noticed a huge gradient of pore pressure on the first elements in contact with microtunnel wall, several mesh sizes are studied to put in evidence whether previous results were perturbed or not by this kind of phenomena. Analysis of water pressure field after 1 week of ventilation is proposed in Figure 28 from meshes corresponding to different degrees of refinement: case (a) is a coarse mesh, case (b) is a middle-size mesh, case (c) in a very fine mesh and case (d) is a coarse mesh which has been strongly refined around borehole wall. Comparison of water pressure evolutions with time at 50cm to microtunnel wall in the horizontal direction (that is to say closed to HG-A3 sensors borehole) for these 4 meshes can be shown in Figure 29.

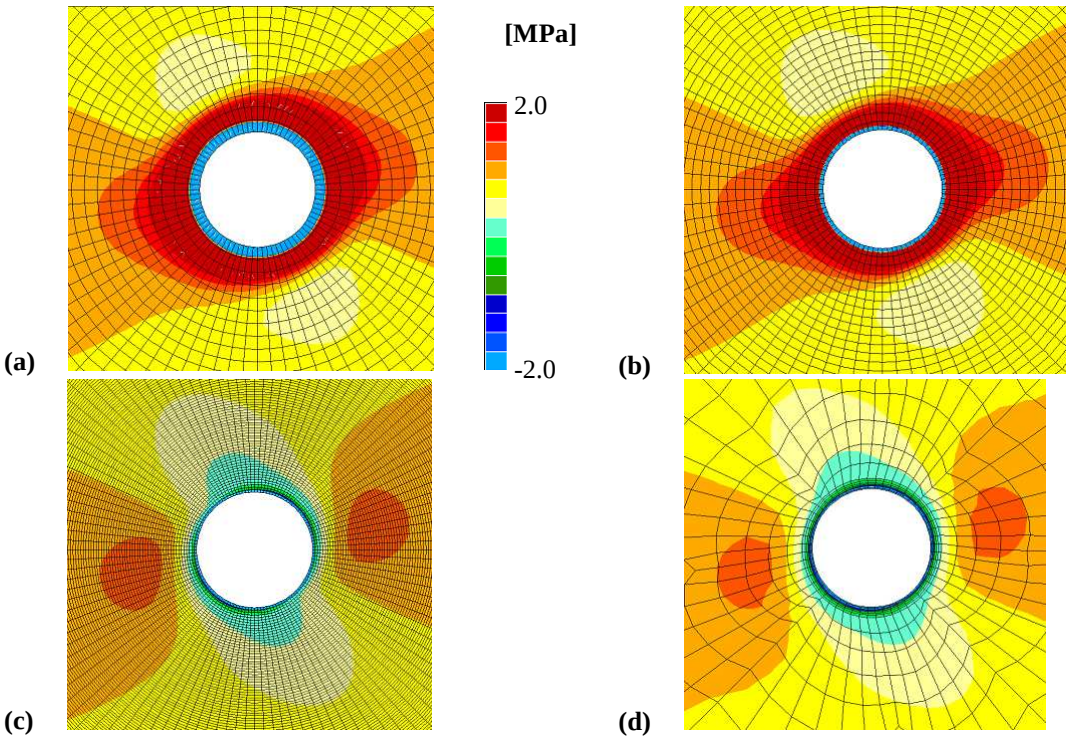

Figure 28: Pore pressure evolution after excavation depending of mesh size

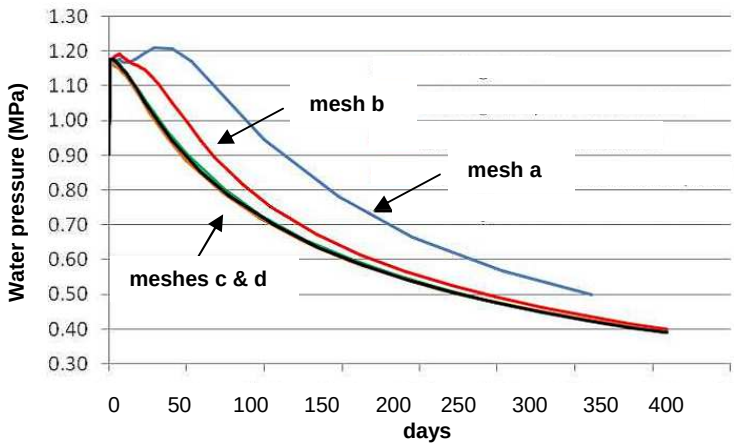

Figure 29: Comparison of water pressure evolutions with time at 50cm to tunnel wall in the horizontal direction (HG-A3) for 4 different meshes

These comparisons permit to illustrate that the global fine mesh (noted c) and the fine mesh around tunnel wall (noted d) provide the same water pressure evolution. On contrary, coarser meshes (noted a and b) provide overpressures with a “late-effect” in time. This confirms that even if in the previous analysis results (summarized in Figure 24) are qualitatively relevant, they are not quantitatively significant. Because of a strong gradient of water pressure close to tunnel wall, finite element model needs to admit a very fine mesh to well analyse the problem. Furthermore, the water pressure level reached does not yet correspond to the measured one. Mesh size is not enough to explain the intensity of the pore water pressure peak.

4.4.2 Influence of the lateral large gallery on HGA modelling

HGA microtunnel is closed and quite parallel to the main Gallery 04 of Mont Terri URL, which has been drilled 8 months before HGA microtunnel (see Figure 30). The short distance between HGA and the Gallery is expected to have effects on pore water pressure field. In fact, initial pore pressure in Mont Terri URL is usually equal to 2MPa, while around HGA microtunnel it has been measured equals to 0.9MPa. By including Gallery 04 in our model (considering a distance between HGA and the Gallery equals to 7.5m – see red box in Figure 30-a), the goal of this section is to evaluate its influence and to show if gallery drainage could explain the low water pressure value. For this, similar hydromechanical loadings than the one used for HGA microtunnel (cf. Figure 13) are imposed to the Gallery with an initial pore water pressure P_w = 2MPa. Ventilation phase is also limited to 8 months.

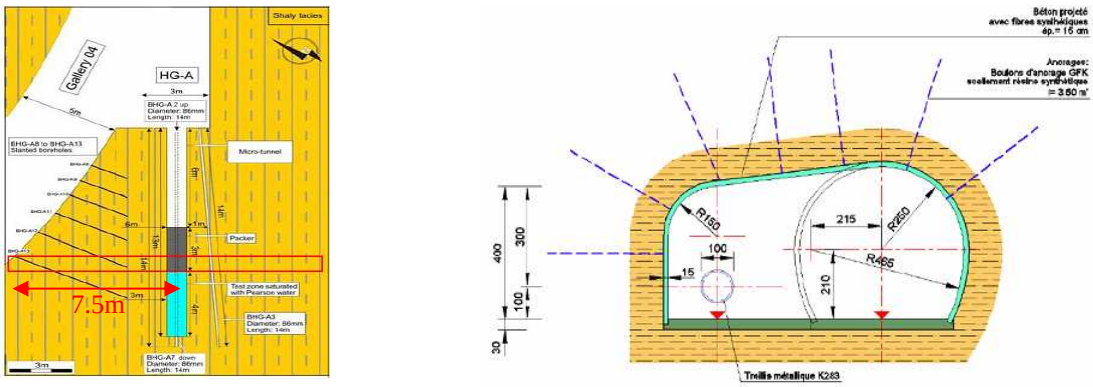

(a) (b)

Figure 30: Views of HGA microtunnel and Gallery04 in Mont Terri URL

<u>Excavation and ventilation of Gallery04 during 8 months</u>

The main effects observed after excavation and ventilation of the Gallery04 are similar to the ones observed previously around HGA tunnel as shown on Figure 31. However, the specific shape of the gallery, provide some additional stress concentrations. Because of the large scale of the excavated Gallery, ventilation and permeability anisotropy do not play a significant role on water pressures. Pressure field shape is not oriented parallel to bedding as around HGA borehole. Nevertheless, its extension is very large and includes microtunnel area, meaning that Gallery04 has an influence on HGA microtunnel environment. After 8 months of ventilation, water pressure in the neighbourhood of HGA microtunnel is around 0.9MPa, which is consistent with the measured value.

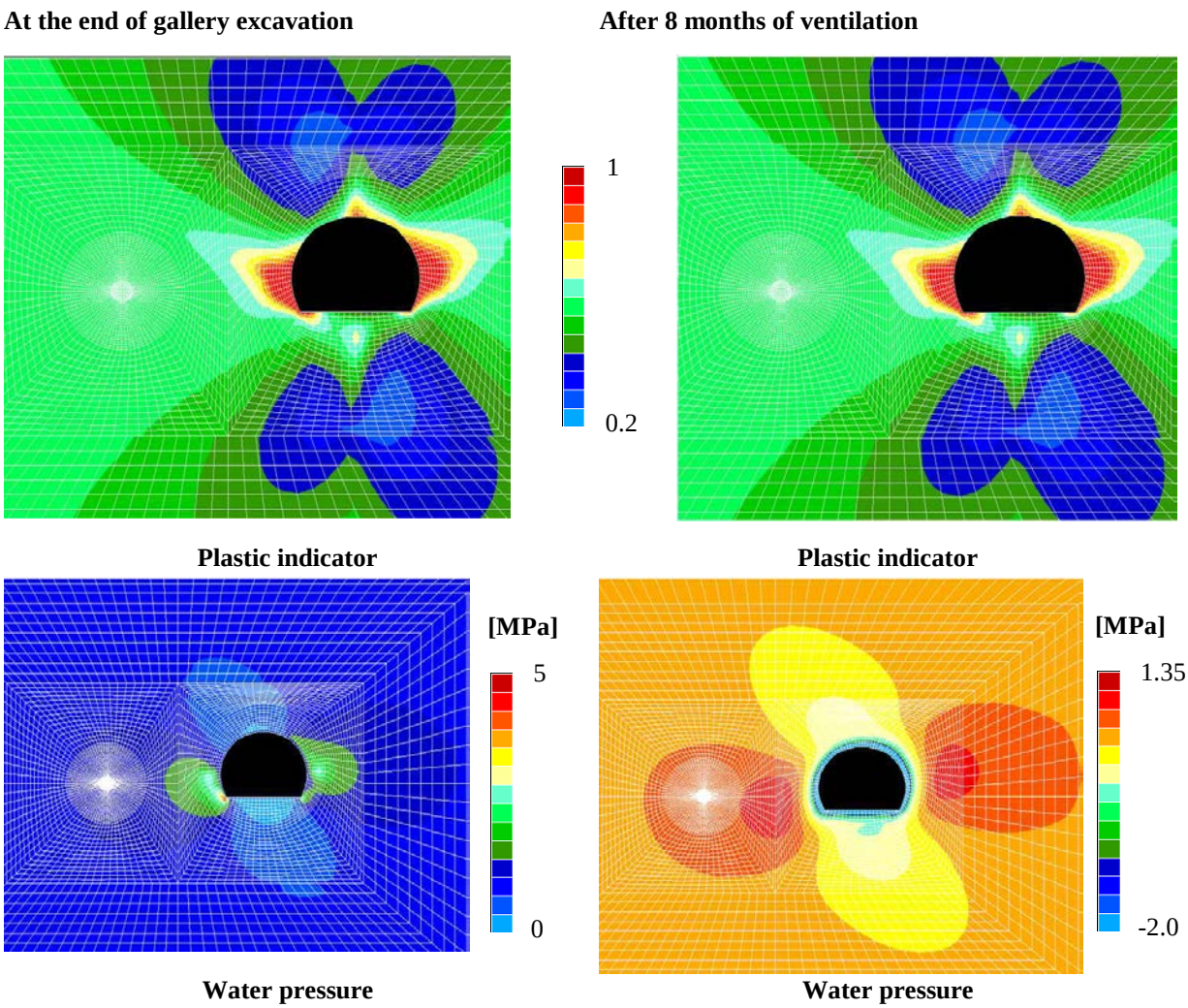

Figure 31: Simulation of Gallery04 before HGA drilling – plastic indicator and water pressure evolutions after excavation and after 8 months of ventilation

Microtunnel modelling

After 8 months of Gallery04 ventilation, HGA microtunnel is drilled. During 10 months, no activity is realised despite tunnel ventilation. So, we propose to extend this period to study ventilation effect on pore water pressure (Figure 32), saturation degree (Figure 33) and plastic indicator (Figure 34) during 8 additional years. Then, Gallery04 ventilation is kept constant whereas the hydromechanical loadings described in Figure 13 are imposed to HGA microtunnel.

Even if qualitatively, results present in Figure 32, Figure 33 and Figure 34 are similar to the previous ones without gallery effects, evolution of water pressures with time (Figure 32) show that gallery excavation and drainage affect the water pressure evolution around the microtunnel area. Microtunnel is on the influence zone of Gallery04 drainage. However, it seems to not have influence on saturation degree; results on Figure 24 and Figure 33 are similar. Plastic indicators are also similar (see Figure 24 and Figure 34): whereas after excavation plasticity appears, during the first year of ventilation plastic indicator decreases. After one year of ventilation, saturated backfill installation keeps impermeable microtunnel wall. Suction is high, saturation degree increases and then plastic indicator evolves to reach a value close to 0.962. As water pressures are less than initial ones, no plasticity appears even after 9 years.

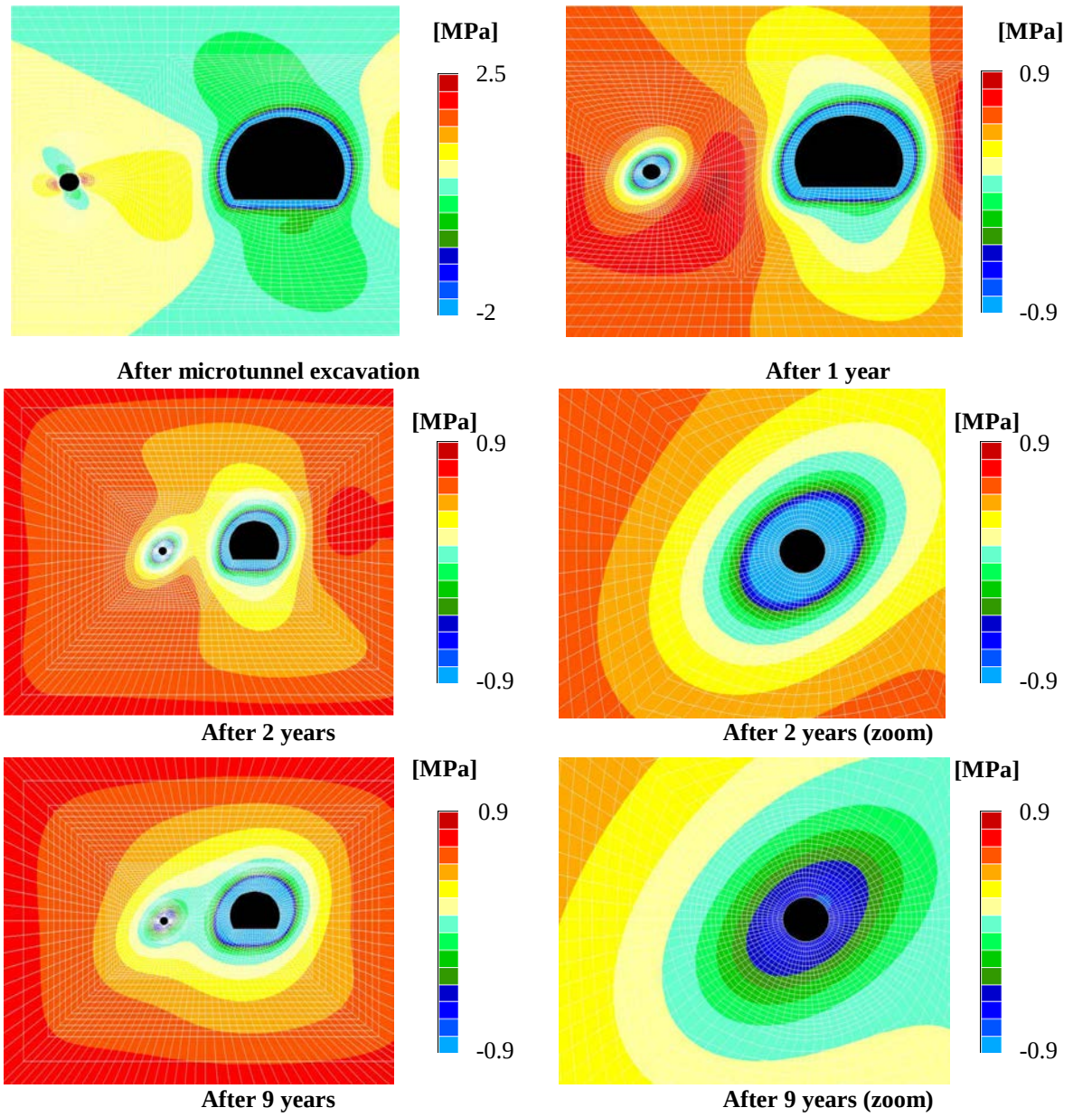

Figure 32: Pore pressure evolutions around gallery04 and HGA microtunnel

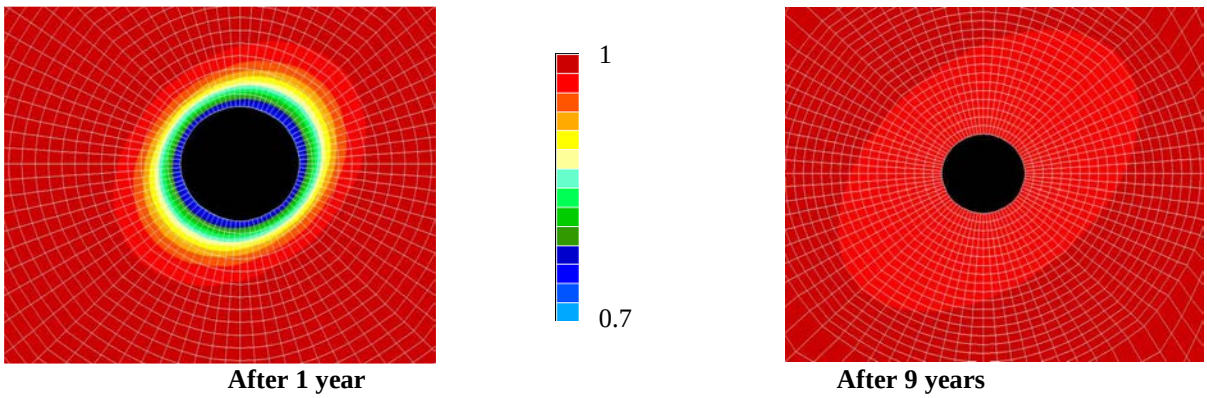

Figure 33: Saturation degree evolutions around HGA microtunnel (modelling accounting gallery effect)

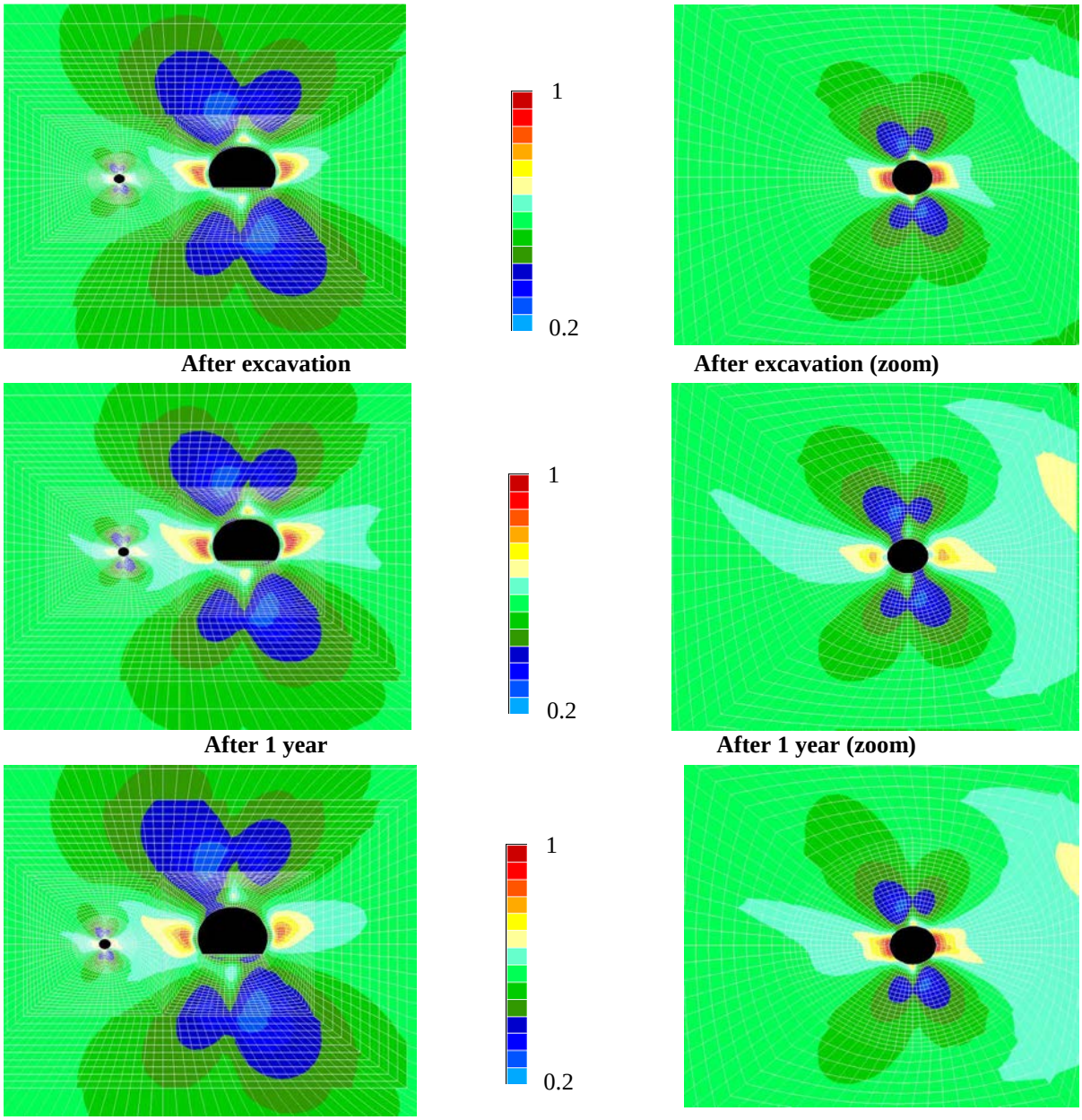

After excavation **After excavation (zoom)**

After 1 year **After 1 year (zoom)**

After 9 years **After 9 years (zoom)**

Figure 34: Plastic indicator evolutions around gallery04 and HGA microtunnel

To conclude, the main effect of Gallery 04 is observed on water pressure evolutions. The measure value of initial pore pressure (before HGA microtunnel excavation) can be explained by Gallery04 drainage. One year after HGA microtunnel excavation, the global pore pressure stays constant and equal to 0.9MPa. However, in the close neighbourhood of HGA microtunnel, pore pressure evolution is not significantly affect by Gallery04 drainage. Its influence is too weak compare to the own microtunnel drainage to play a significant additional role on water pressure evolutions. Then, one can assume that it is not necessary to consider Gallery04 in the following.

4.4.3 Influence of the tectonic fault

In situ observations have shown that the rock collapses in the top-left side of HGA borehole (Figure 26). This large damage is expected to be the consequence of stress concentrations in relation with anisotropy combining with the presence of a tectonic fault weakening the rock in a direction subparallel to bedding. To clearly put in evidence the effects of this kind of fault, we propose in this section to include it in the finite element model.

Due to the lack of information about the tectonic fault, this one is expected to be oriented at 45° (as bedding plane) in a distance equals to 0.19m from HGA borehole wall. The fault is characterized by interpenetration and friction coefficients (following Coulomb law) in case of contact between the two fault borders, and by transverse and longitudinal permeabilities. Parameters are given in

Table 4.

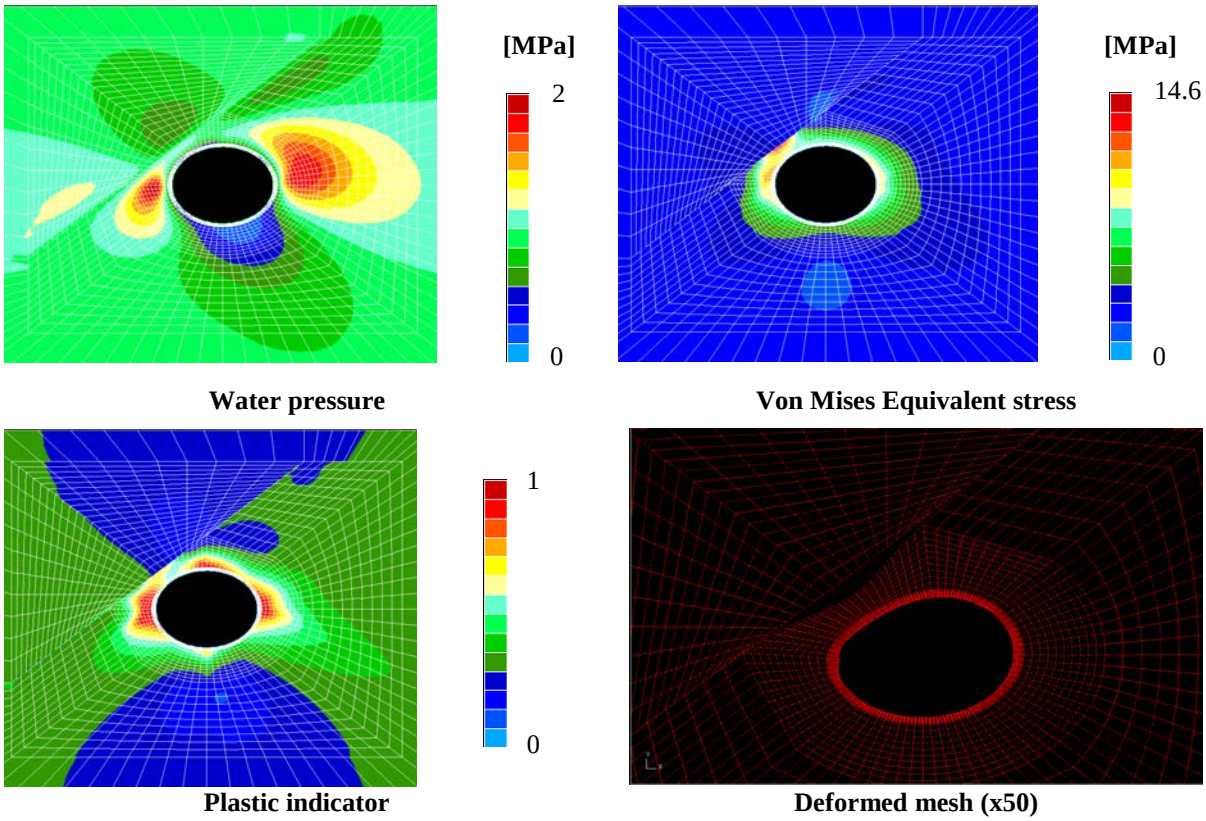

Figure 35: Influence of tectonic fault around HGA borehole

Table 4: Tectonic fault characteristics

Penalty coefficient on contact pressure	[GPa]	K_p	3
Penalty coefficient on shear stress	[GPa]	K_τ	3
Friction angle	[-]	$tan\ \Phi$	0.37
Longitudinal permeability	[m²]	$K_{l,int}$	2.10^{-15}
Transverse transmissivity in case of contact	[m².s^{-1}]	$T_{t,c}$	1.10^{-5}
Transverse transmissivity without contact	[m².s^{-1}]	$T_{t,nc}$	1.10^{-5}
Porosity	[-]	n_f	0.13

The fault introduces a high permeability which has a strong effect on water pressure field as shown in Figure 35. Moreover, the presence of the fault closed to borehole wall provides some additional overpressures in stress field. Due to excavation, the fault opens. It results an increase of equivalent stress (in Von Mises definition) between fault and HGA borehole that generates more plasticity after excavation compared to Figure 24. In means that the solicitation of the zone between fault and HGA borehole is higher than everywhere around the tunnel amplifying the damage as observed in Figure 26.

4.4.4 Introduction of an artificial EDZ around HGA borehole

The previous checking on the influences of mesh size, the presence of the main Gallery and the presence of a tectonic fault have permitted to confirm some observations made in situ around HGA borehole but are not sufficient to perform an accurate modelling of the experiment satisfying the comments made on section 4.3.2. Then, as tunnel drilling provides stress redistribution and damage (microcracking), which reduce rock strength and increase permeability in a borehole surrounding area corresponding to the Excavation Damaged Zone, we propose to introduce an artificial EDZ in the model.

Thanks to an “extended” analogy between damage and plasticity, EDZ is defined as an ellipsoid including area around tunnel where plastic indicator PI > 0.5. It corresponds to an ellipsoid centred on tunnel axis, for which the larger half-axis is around 1m long oriented horizontally and the smaller half-axis is closed to 0.6m long as proposed in Figure 36. As a first approximation of the EDZ, Young modulus anisotropic values are divided by 10, whereas permeability anisotropic values are multiplied by 10^5 inside the EDZ compare to Table 3. These choices are made a priori, in reference to Selfrac experiment observations (Bernier et al. 2007, Levasseur et al. 2010), in order to permit to identify qualitatively the effects of EDZ on the modelling. Calibrations will be the object of the next section page 43.

Before that, notice that the wanted goals with EDZ are numerous and various. In fact, decreasing the EDZ stiffness should modify stress and strain fields. Deformed mesh after excavation should be more important; stress overpressures should be noticed in a larger zone than EDZ. Moreover, because of the ellipsoid shape of EDZ, additional stress concentrations have to become visible on external borders of EDZ due to its strong curvature. Furthermore, by increasing strongly the permeability in EDZ, it becomes more permeable, reducing the water overpressures after excavation and transferring suction effects on the boundary between EDZ and undamaged rock during the ventilation phase.

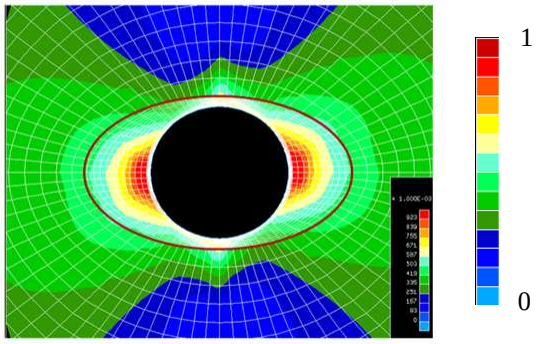

Figure 36: Excavation Damaged Zone definition around HGA borehole based as an ellipsoid including area around tunnel where plastic indicator PI > 0.5

Influence of EDZ on excavation phase

Comparison between modelling with or without EDZ is presented in Figure 37 on water pressure field, plastic indicator field and deformed mesh after excavation phase. In the simulation with EDZ, we observe as expected a weak water pressure inside the EDZ due to high permeability. The zones with high water pressures are more extended in the simulation with EDZ than in the simulation without EDZ. It results a modification of stress field and two high values in the plastic indicator field in horizontal directions. More precisely, unloading due to excavation leads to vertical strains larger than the horizontal ones at the interface between intact rock and EDZ. Then, rock is in compression along larger ellipsoid axis because of EDZ contraction. This contraction can be explained by a decrease of water pressure in EDZ, in which permeability is very high. However, plastic indicator level is globally smaller around the borehole in the simulation with EDZ, meaning that no additional plasticity (or damage) is generated by the presence of EDZ. Convergence of the excavation also increases by taking into account the EDZ. Deformed mesh orientation is slightly modified due to combined effects of deformations inside and outside EDZ (deformations inside the EDZ are more influenced by bedding than deformations outside the EDZ because of higher permeability).

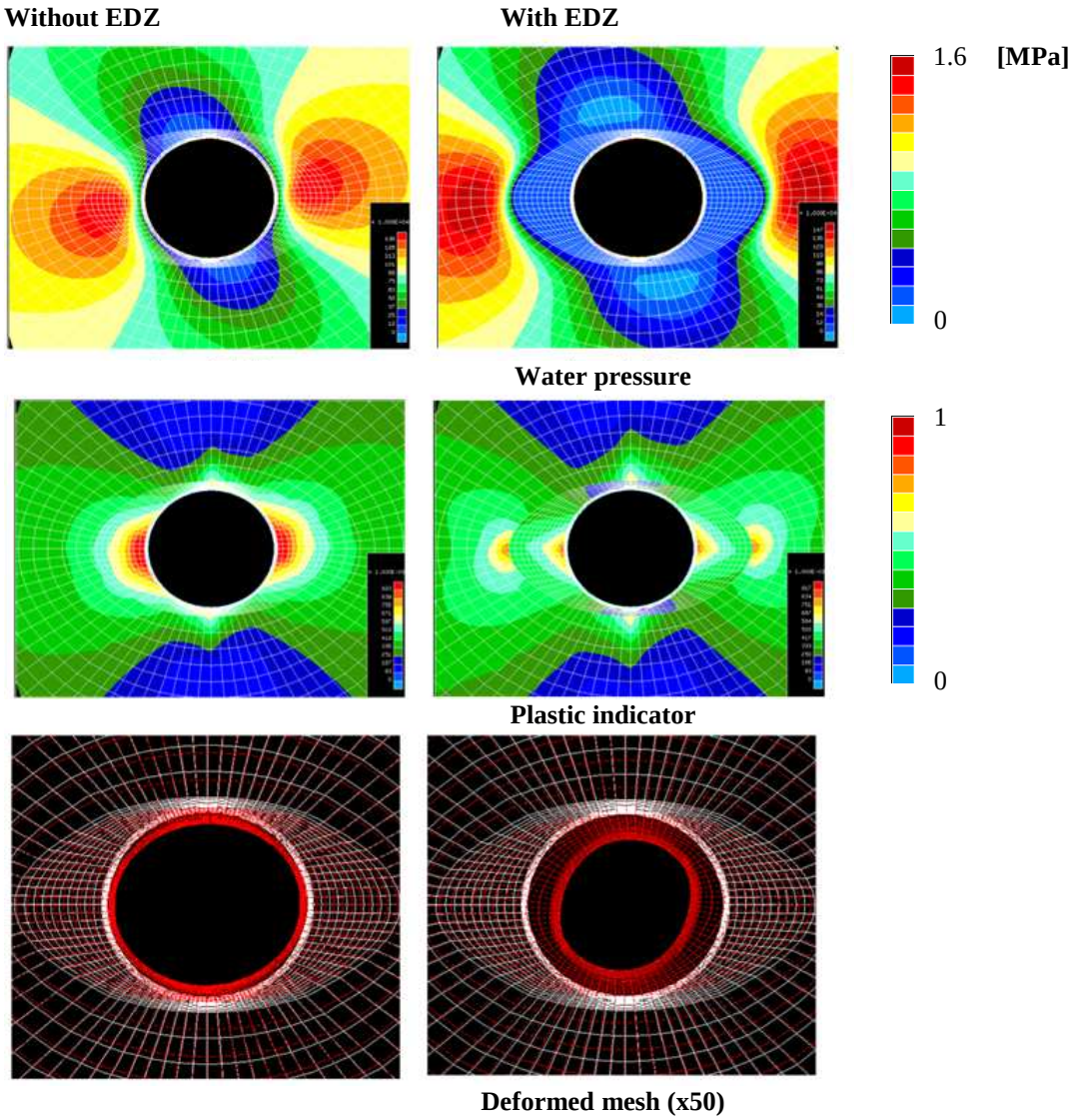

Figure 37: Influence of EDZ at the end of excavation phase

Influence of EDZ on ventilation phase

The same analysis is performed in Figure 38 on results given after ventilation phase. We can notice that in simulations with or without EDZ, suction is observable in quite similar directions close to bedding plane. It means that even if EDZ is oriented horizontally, drainage is influenced by permeability anisotropy at 45°. However, by taking into account of an EDZ with high permeability, damaged rock in EDZ is quickly unsaturated due to ventilation. Suction effects are transferred on the EDZ external borders and affect the rock on a larger zone around borehole. It results a strong modification of deformed mesh, which becomes ellipsoidal after ventilation in the presence of EDZ compare to the case without EDZ. The imposed suction "squashes" the EDZ and generates additional stress concentrations at the extremity of ellipsoid larger axis, modifying the plastic indicator field. However, like previously, plastic indicator level is less than 1 and globally smaller around the borehole than in the simulation without EDZ, meaning that no plasticity (or damage) is generated by the presence of EDZ during ventilation.

All these phenomena seem to be representative to what has been observed in situ around HGA borehole. Then, one can conclude that adding artificial EDZ around HGA borehole in FE modelling should be considered to explain the water pressure and displacement evolutions observed in situ (Figure 15). The next section 4.5 will be dedicated to its calibration.

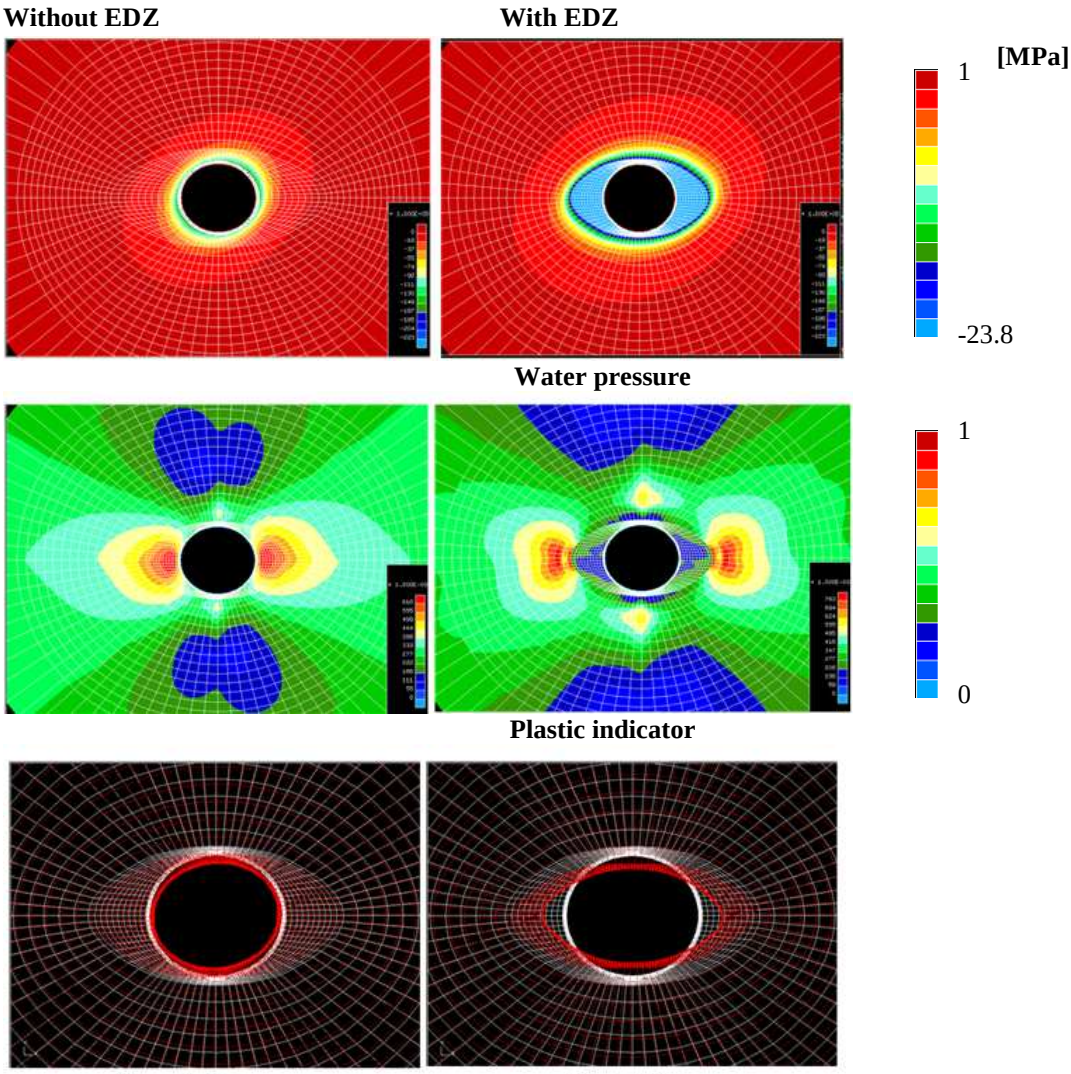

Figure 38: Influence of EDZ after ventilation phase

4.5 Calibration on experimental results

Results presented in section 4.4.4 have shown that considering EDZ around HGA borehole is the most relevant approach to model the experiment. However, the properties of the model are not well known and can not be easily obtained from in situ observations. Then, we propose to base the calibration (given in section 4.5.3) on the analysis of the influences of different factors on the evolution with time of water pressure measured by sensor B-A03PE3 (located approximatively at 1m to the left size of HGA borehole wall) and of displacements measured by B-A05DE07 (located approximatively at 1m above HGA borehole wall – see Figure 14 and Figure 15). These factors mainly concern EDZ properties and undamaged Opalinus Clay properties. For this, let's start with a priori initial calibration proposed previously and summarized in Table 5. All the other parameters are fixed following values given in Table 3.

Table 5: Initial calibrations

	1st calibration	
	Outside EDZ	**Inside EDZ**
$E_{//}$ [GPa]	4.4	0.44
$E_{\perp}$ [GPa]	3.3	0.33
$k_{sat\,//}$ [m²]	2.10^{-20}	2.10^{-15}
$k_{sat\,\perp}$ [m²]	8.10^{-21}	8.10^{-16}
	EDZ ellipsoid size	
***a* - Larger half-axis [m]**	1	
***b* - Smaller half-axis [m]**	0.6	

4.5.1 Influence of EDZ properties

Influence of EDZ size

According to Figure 37, the maximum of water pressure appears after excavation close to the extremity of EDZ-ellipsoid larger axis due to stress concentration resulting from ellipsoid strong curvature. Then, depending of the axis length, the peak of water pressure can be modified. Figure 39 presents water pressure evolution with time for several sets of ellipsoid size (characterized by the largest half-axis named *a* and the smallest half-axis named *b*) compared to in situ measurements. This figure shows that for the largest half-axis *a*, the water pressure peak is the smallest because it probably not correspond to the maximal value reached by water overpressure. On contrary, for the smallest half-axis *a*, the water pressure peak is the highest because it could correspond to the maximal value reached by water overpressure. It is also important to notice that variations of half-axis *a* are small, meaning that this parameter is very sensitive on numerical results. On contrary, half-axis *b* seems to have a weak influence on water pressure peak and will not influence too much the calibration. These remarks on water pressure evolutions confirm that adding artificial EDZ around HGA borehole in FE modelling is a good issue to explain observations and improve calibration. Moreover, it permits to introduce a realistic delay in the apparition of water pressure peak, which was inexistent in Figure 27 representing a simulation results in a case without EDZ.

In term of displacements, the presence of an EDZ influences the vertical borehole convergence. Figure 39 presents displacement evolutions with time for the sets of ellipsoid size compared to in situ measurements. This figure shows that displacements increase with

the decrease of the largest half-axis *a*. However, like previously half-axis *b* seems to have a weak influence on water pressure peak and does not influence too much the calibration.

Finally, according to these observations, it seems that to provide a good calibration on both water pressures and displacements a good compromise can be obtained from an ellipsoid size defined as: *a* = 1.05m and *b* = 0.6m. However, this definition of the EDZ size has to be taken carefully because of its strong effect on numerical results. A comparison with in situ EDZ estimation is essential to confirm its relevancy.

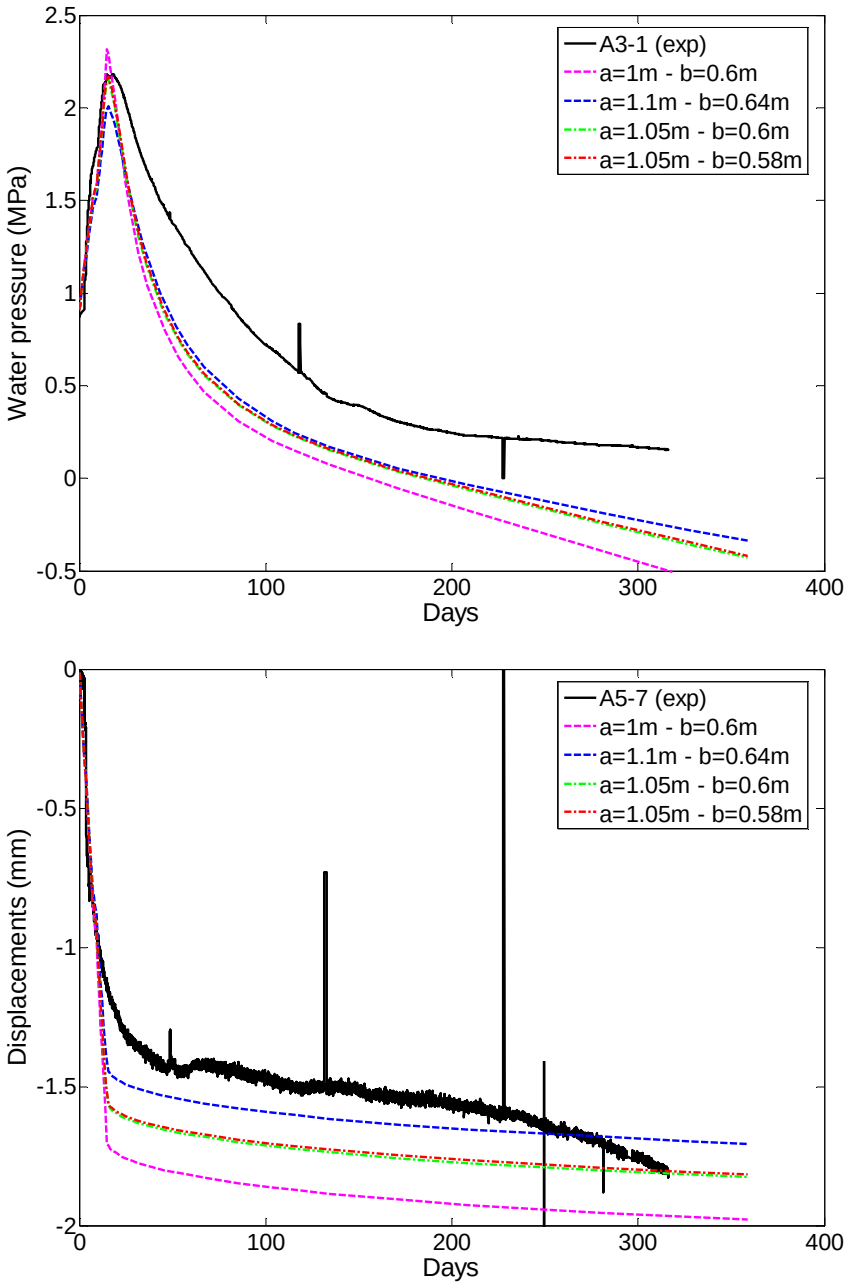

Figure 39: Influence of EDZ size on water pressure and displacement evolutions with time

Influence of elastic modulus in EDZ

Figure 40 shows that the degradation of elastic modulus in EDZ has an impact on water pressure and displacement evolutions with time. In this figure, two cases are considered for which elastic modulus in EDZ are divided by 5 ($E_{//}$ = 0.88GPa and $E_{\perp}$ = 0.66GPa) or by 10 ($E_{//}$ = 0.44GPa and $E_{\perp}$ = 0.33GPa) compared to anisotropic Young modulus in undamaged rock. It appears that when modulus are high (E/5 in EDZ), EDZ is rigid and then displacements are limited and water pressure peak is reduced due to restricted stress concentrations. According to these observations, a significant elastic modulus degradation in EDZ is necessary to fit the peak of water pressure.

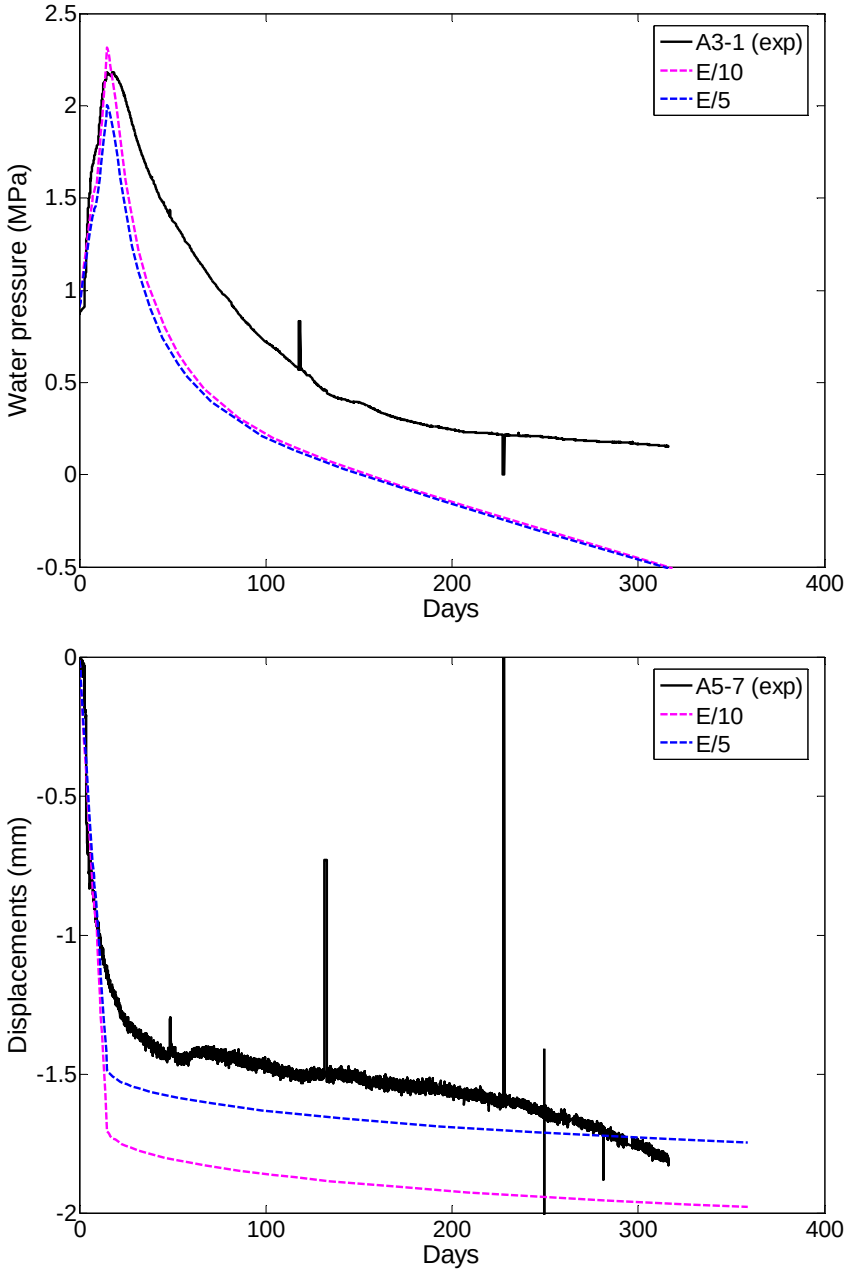

Figure 40: Influence of Young modulus in EDZ on water pressure and displacement evolutions with time

Influence of permeability coefficients in EDZ

Figure 41 shows that the increase of permeability in EDZ due to rock degradation has mainly an impact on water pressure evolution with time whereas displacements are weakly influenced. In this figure, three cases are considered for which permeability coefficients in EDZ are multiplied by 10^3, 10^4 or by 10^5 compared to anisotropic permeability coefficients in undamaged rock. It appears that when permeability is high, rock in EDZ is quickly unsaturated by ventilation and then suction effects are transferred on the EDZ external borders to affect the rock on a large zone around borehole as shown in Figure 38. It results a larger peak of water pressure. According to Figure 41, this phenomenon can be observed since permeability in EDZ reachs a threshold value 10^4 times upper than the undamaged permeability. Then, permeability coefficient is a second parameter that permits to fit the peak of water pressure.

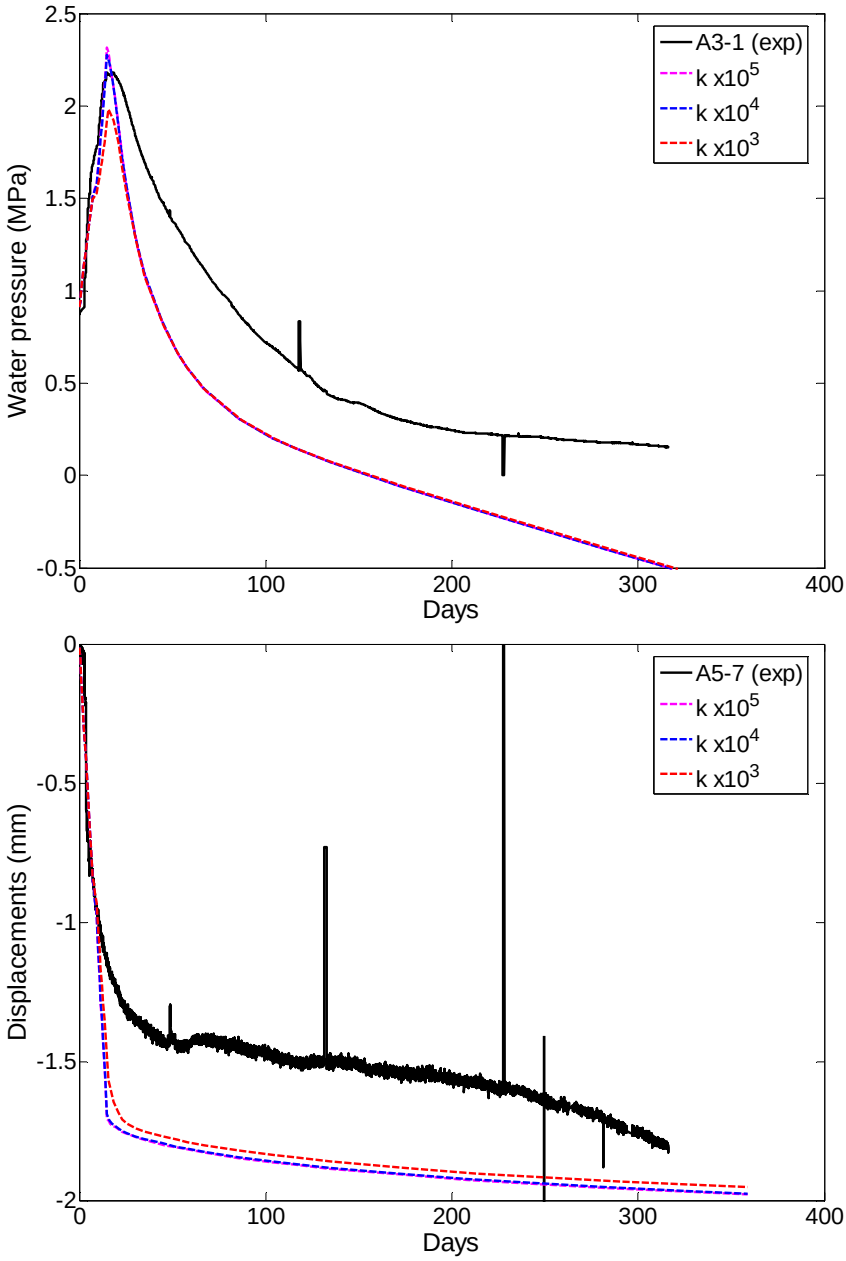

Figure 41: Influence of permeability in EDZ on water pressure and displacement evolutions with time

4.5.2 Influence of undamaged Opalinus Clay properties

Influence of exchange conditions during ventilation phase

Figure 41 shows that EDZ permeability plays a small effect on displacements outside the EDZ and for permeability values lower than a threshold value it does not affect water pressure evolutions. Nevertheless, permeability plays a role on transitional behaviour that can be noticed between excavation and ventilation phases: water pressure peak is delayed with permeability and we observe a smooth evolution of displacements before reaching the plateau. These phenomena linked to permeability variations characterize exchange conditions between the air inside borehole and the rock. Numerically, the simulation of exchange conditions during ventilation phase can be influenced by vapour exchange conditions: by a direct application of suction (estimated from ventilation conditions) or by controlling fluid flows on borehole walls (that permits to apply more slowly the suction as described below). According to our knowledge on Opalinus Clay and to FORGE experimental data, it is not so evident to quantify vapour transfers at rock interface then we propose in this study to analyse its effect on water pressure results.

Hydraulic boundary conditions for exchanges at a gallery wall

In the finite element code LAGAMINE, a non classical boundary condition with water and vapour exchanges exists to impose relative humidity and to model the exchanges between the cavity and the rock (Gerard et al. 2008). This condition implies that two modes of exchange can occur in ventilated cavities allowing flow of water from the ground to the microtunnel if the pore pressure of the ground is higher than the imposed pore pressure at the microtunnel wall and restricting flow of water from the microtunnel to the ground if not (Ghezzehei et al. 2004). The total water flow boundary condition is expressed as the sum of a seepage flow and a vapour exchange flow:

$$\overline{E} = \overline{S} + \overline{q} \tag{4-2}$$

The seepage flow occurs if pore water pressure in the gallery wall rock is larger than cavity air pressure. It is introduced in a finite element code by the function:

$$\begin{cases} \overline{S} = K(p_w^{\Gamma} - p_{atm})^2 & \text{if } p_w^{\Gamma} \geq p_w^{air} \text{ and } p_w^{\Gamma} \geq p_{atm} \\ \overline{S} = 0 & \text{if } p_w^{\Gamma} < p_w^{air} \text{ or } p_w^{\Gamma} < p_{atm} \end{cases} \tag{4-3}$$

with p_w^{Γ} the pore water pressure in the rock formation, p_w^{air} the water pressure corresponding to the relative humidity in the cavity air, p_{atm} the atmospheric pressure and K a penalty coefficient for seepage. p_w^{air} is obtained using Kelvin's law implying that the total suction is equal to the matric suction, without considering osmotic suction.

The vapour exchange mode assumes the existence of a boundary layer on the cavity porous surface (Ghezzehei et al. 2004). It occurs if a difference between vapour densities exists between the rock and the cavity air (Ben Nasrallah & Pere 1988):

$$\overline{E} = \alpha(\rho_v^{\Gamma} - \rho_v^{air}) \tag{4-4}$$

with ρ_v^{Γ} and ρ_v^{air} the vapour density respectively in the rock formation and in the cavity and α a vapour mass transfer coefficient.

Influence of vapour mass transfer coefficient

Then, by considering these seepage elements on the microtunnel wall, effects of vapour mass transfer coefficient α on water pressure evolution during HGA ventilation is studied. The penalty coefficient for seepage K is fixed to 10^{-11}. Three values of α are considered (α = 0.1, 0.01 and 0.001) and compared to the solution for which suction is directly applied to borehole wall. Figure 42 shows that more the condition of fluid flow are restrictive (α is small), lower is the desaturation of EDZ during ventilation. It limits suction effects outside the EDZ, reducing the peak of water overpressure measured by A3 borehole sensors. On contrary, when vapour mass transfer coefficient is high (α=0.1), the solution tends to be equivalent to the case without any condition on fluid transfer. Furthermore, whatever is the condition considered on fluid transfer, no significant effect can be noticed on water pressure evolution after the peak.

These observations confirm that suction effects may quickly reach the undamaged zone and previous assumption of a highly perturbed EDZ is reliable. Nevertheless, if the behaviour around peak overpressure can be well capture by the proposed approach, it still misses the water pressure decreasing observed during the year of ventilation. To improve this, let's see the effects of permeability outside the EDZ.

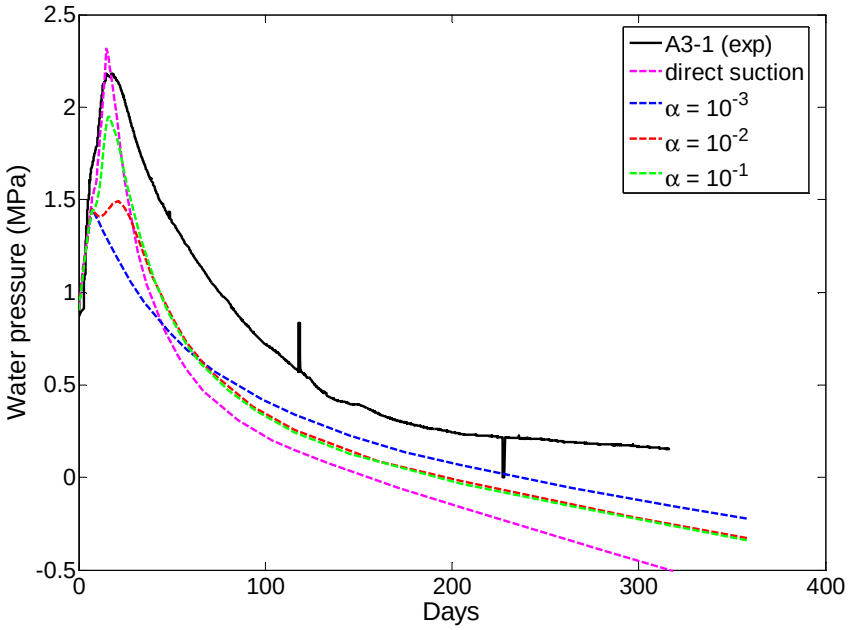

Figure 42: Influence of vapour mass transfer coefficient on water pressure evolutions with time

Influence of permeability coefficients outside EDZ

All the previous results show that the overpressure peak and delay can be estimated by adjusting EDZ properties, but modelling still misses to capture the decrease of water pressure observed during ventilation. As sensors are placed outside EDZ, the decrease of water pressure should be link to undamaged rock permeability. Figure 43 presents the influence of permeability coefficients outside EDZ. Three cases are considered: with the undamaged values (K_{out}) or with values equal to anisotropic permeability coefficients in undamaged rock divided by 2 or by 1.5. It appears that more the permeability outside EDZ is small, more the decrease of water pressure is slow, permitting a better water pressure decrease calibration.

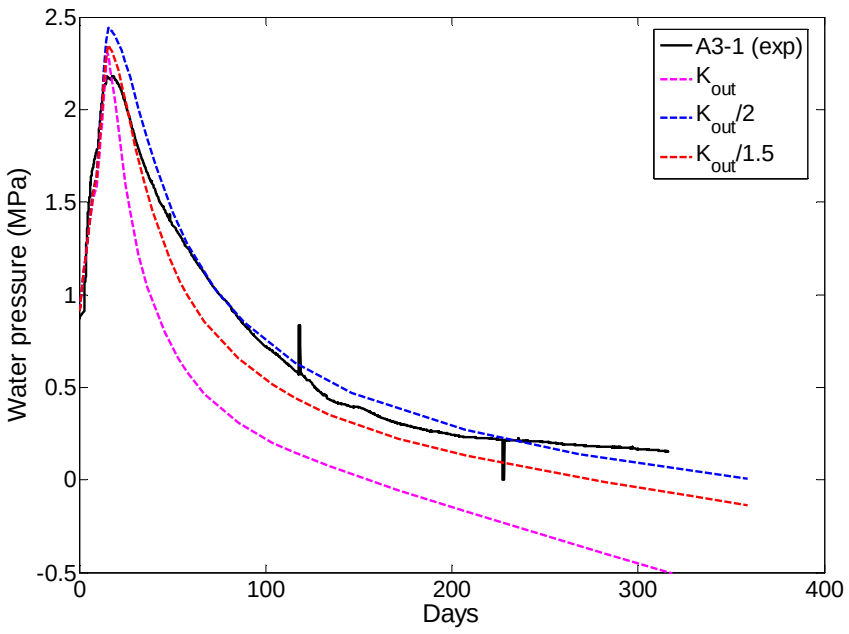

Figure 43: Influence of permeability outside EDZ on water pressure evolutions with time

4.5.3 Final calibrations

Calibration based on pore water pressure evolution

According to all the previous results and comments, calibrations can be done for each water pressure evolution by adjusting Young modulus in EDZ and permeability inside and outside the EDZ. Figure 44 to Figure 47 show that it is possible to obtain a good fit of most of the experimental curves (water pressure measured by sensors B-A03PE1, B-A03PE2, B-A03PE3 and B-A02PE2 – see Figure 14) by considering (1) the parameters summarized in

Table 6, (2) an elliptic EDZ size defined as: a = 1.05m and b = 0.6m, and (3) by allowing fast vapour transfers. Fittings proposed in these figures slightly change from one borehole calibration to another one. Then, we suggest averaging the parameter values to complete the calibration as proposed in Figure 48.

Table 6: Young modulus and Permeability calibrations

	Calibration of B-A03PE1 (Figure 44)		**Calibration of B-A03PE2** (Figure 45)		**Calibration of B-A03PE3** (Figure 46)		**Calibration of B-A02PE2** (Figure 47)		**Averaged Calibration** (Figure 48)	
	Outside EDZ	**Inside EDZ**	**Outside EDZ**	**Inside EDZ**	**Outside EDZ**	**Inside EDZ**	**Outside EDZ**	**Inside EDZ**	**Outside EDZ**	**Inside EDZ**
$E_{//}$ [GPa]	4.4	0.88	4.4	0.44	4.4	0.44	4.4	0.44	4.4	0.66
$E_{\perp}$ [GPa]	3.3	0.66	3.3	0.33	3.3	0.33	3.3	0.33	3.3	0.50
$k_{sat //}$ [m²]	10^{-20}	2.10^{-15}	$1.3\ 10^{-20}$	2.10^{-15}	10^{-20}	2.10^{-15}	10^{-20}	2.10^{-15}	$1.15\ 10^{-20}$	2.10^{-15}
$k_{sat \perp}$ [m²]	4.10^{-21}	8.10^{-15}	$5.3\ 10^{-21}$	8.10^{-15}	4.10^{-21}	8.10^{-15}	4.10^{-21}	8.10^{-15}	$4.65\ 10^{-21}$	8.10^{-15}

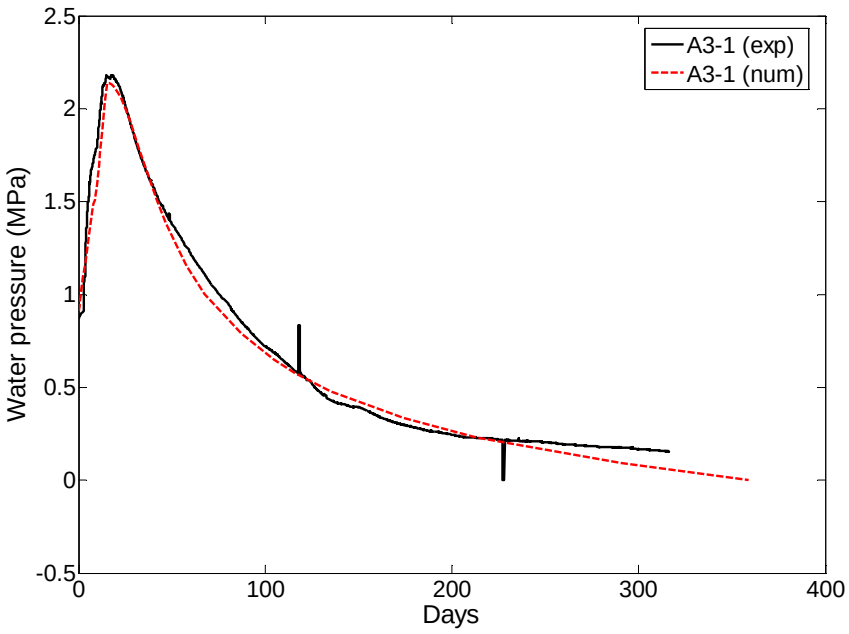

Figure 44: Calibration of B-A03PE1 water pressure evolutions with time

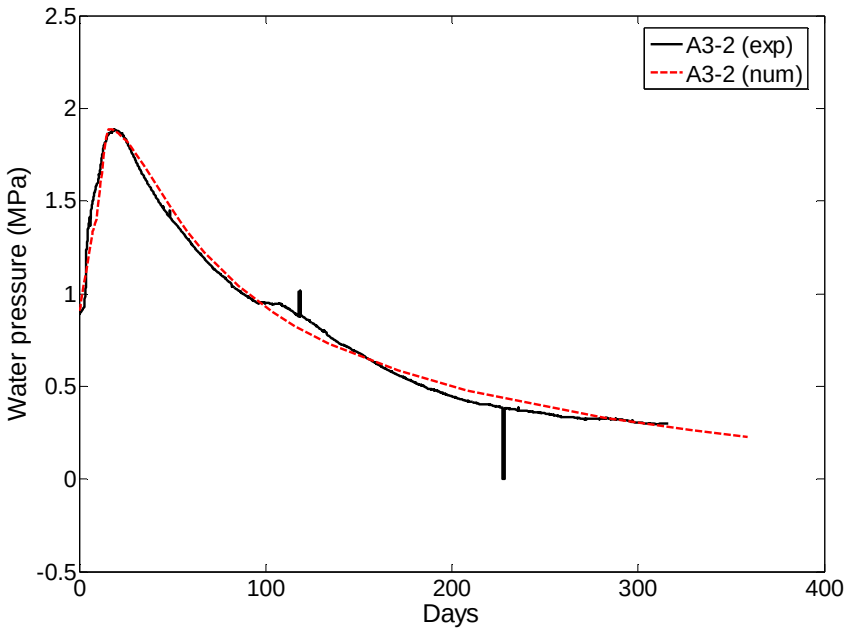

Figure 45: Calibration of B-A03PE2 water pressure evolutions with time

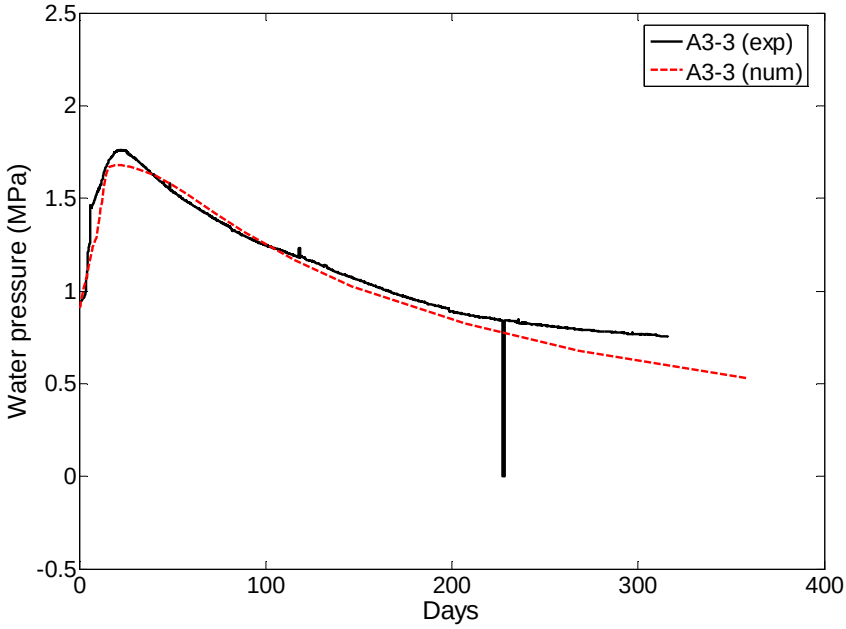

Figure 46: Calibration of B-A03PE3 water pressure evolutions with time

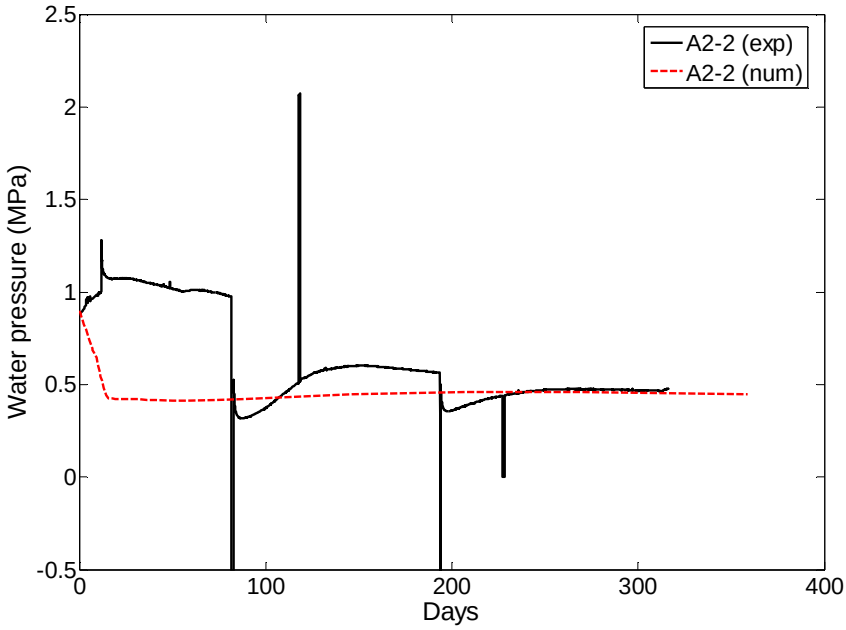

Figure 47: Calibration of B-A02PE2 water pressure evolutions with time

By averaging the parameter values, Figure 48 presents an averaged calibration. Then, we observed a rapid increase of pore water pressure in sensor HG-A3 while sensors HG-A2 measures a slight increase of pore water pressure. This difference in the pore water pressure response according to the radial direction of observation is due to the different sources of anisotropy (elastic, plastic, hydraulic and stress state). The main contribution of this difference is probably the anisotropy of the stress state. Vertical stress being much higher than horizontal stress, the gallery wall displacement is higher in the vertical direction, inducing a dilation of pore space along with a decrease of pore water pressure (sensor HG-A2). On the contrary, in the horizontal direction (sensor HG-A3), the behaviour is more compressive, inducing drastic increase of the pore water pressure. The proposed 2D plane strain numerical simulation is able to reproduce these main trends of pore water pressure evolutions. The

introduction of a horizontal EDZ around HGA borehole permits to well capture the magnitude of the peak and the decrease which follows in the pore water pressure evolution measured by sensor HG-A3. The experimental measurement of the pore water pressure in sensor HG-A2 shows a slight increase of pore water pressure until 50 days after excavation while the numerical modelling predicts an immediate decrease of the pore water pressure. Nevertheless, at long-term the same magnitude is reached. However, total displacements of sensor HG-A5 (1m above the gallery) and HG-A7 (1m below the excavation) show that after an immediate displacement 0.5mm, the displacements continue to increase due to consolidation processes. If the 2D plane strain numerical simulation is able to capture immediate response, the subsequent evolution of the displacements is slightly overestimated. The modelled displacements in sensor HG-A5 and HG-A7 are opposite in sign and not totally equal. Anisotropies considered in the model capture differences in these symmetric orientations but is not sufficient to reproduce displacement evolutions.

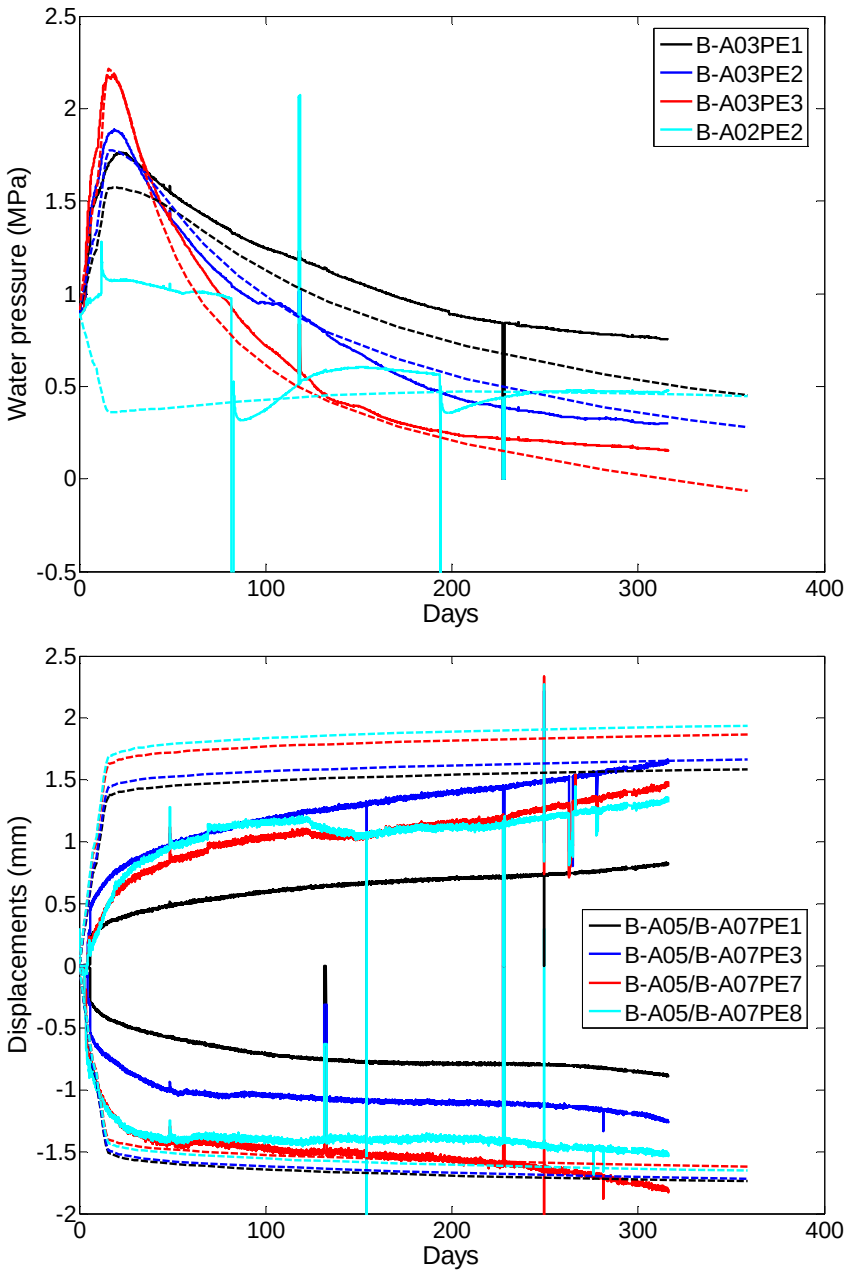

Figure 48: Calibration of water pressure and displacements evolutions with time (mainly based on pore water pressure evolution)

Calibration based on displacement evolutions

In order to improve displacement evolution calibration, we propose to modify elastic modulus. Instead of considering the values of the anisotropic Young moduli of intact rock (outside EDZ) deduced from triaxial calibrations, we propose to fix them to the values commonly admitted in literature: $E_{//}$ = 10GPa and $E_{\perp}$= 4GPa. Inside the EDZ, Young modulus and permeability are still equal to parameters given in

Table 6. This assumption supposes that parameters deduced from triaxial tests correspond to alterated parameters and are not enough representative of the intact rock. By this way, water pressure evolutions still reproduce peak magnitudes in average but do not capture anymore the decrease of water pressure observed during ventilation. Furthermore, displacement curves are this time underestimated as shown in Figure 49.

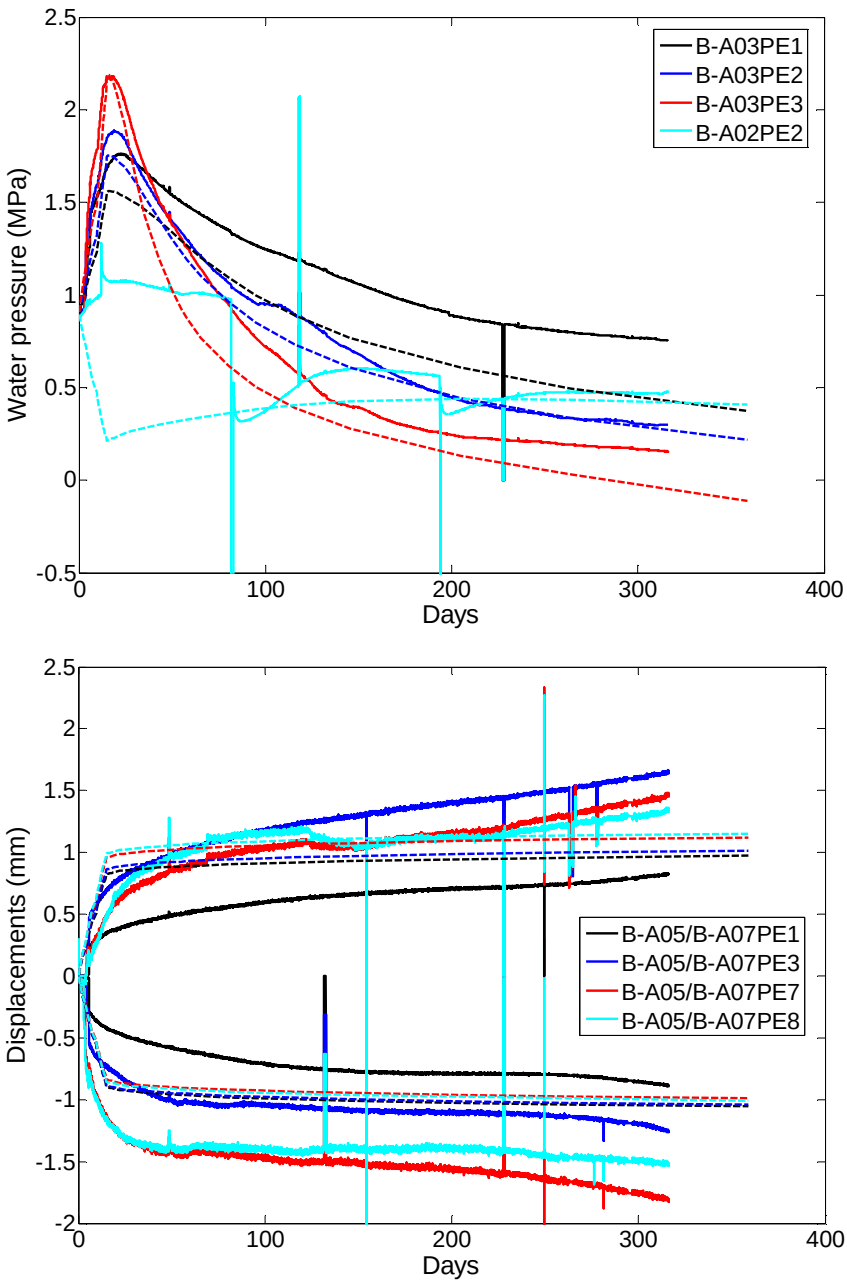

Figure 49: Calibration of water pressure and displacements evolutions with time (mainly based on displacement evolutions)

However, by considering an average calibration between the one given in Figure 48 and Figure 49, for which $E_{//}$ = 7GPa and $E_{\perp}$= 3.5GPa, a good compromise can be obtained as shown in Figure 50.

Then, even if the 3D complex geometry of the system has been simplified into a 2D plane strain problem, the general trends of numerical results, obtained from parameters detailed in Table 7, are in very good agreement with experimental measurements. Nevertheless, these results have to be carefully taken into account. In 2D simulation, neither the effects of the impervious liner installed in the 6 first meters of the gallery nor the effects of excavation steps have been considered, even though they should have mechanical and hydraulic consequences on the global hydro-mechanical response. Moreover, all the sensors that are located in a 3D space have been projected in the 2D modelled plane, neglecting their longitudinal location. These assumptions let think that 2D plane strain model is still uncertain and need to be completed by a future 3D modelling.

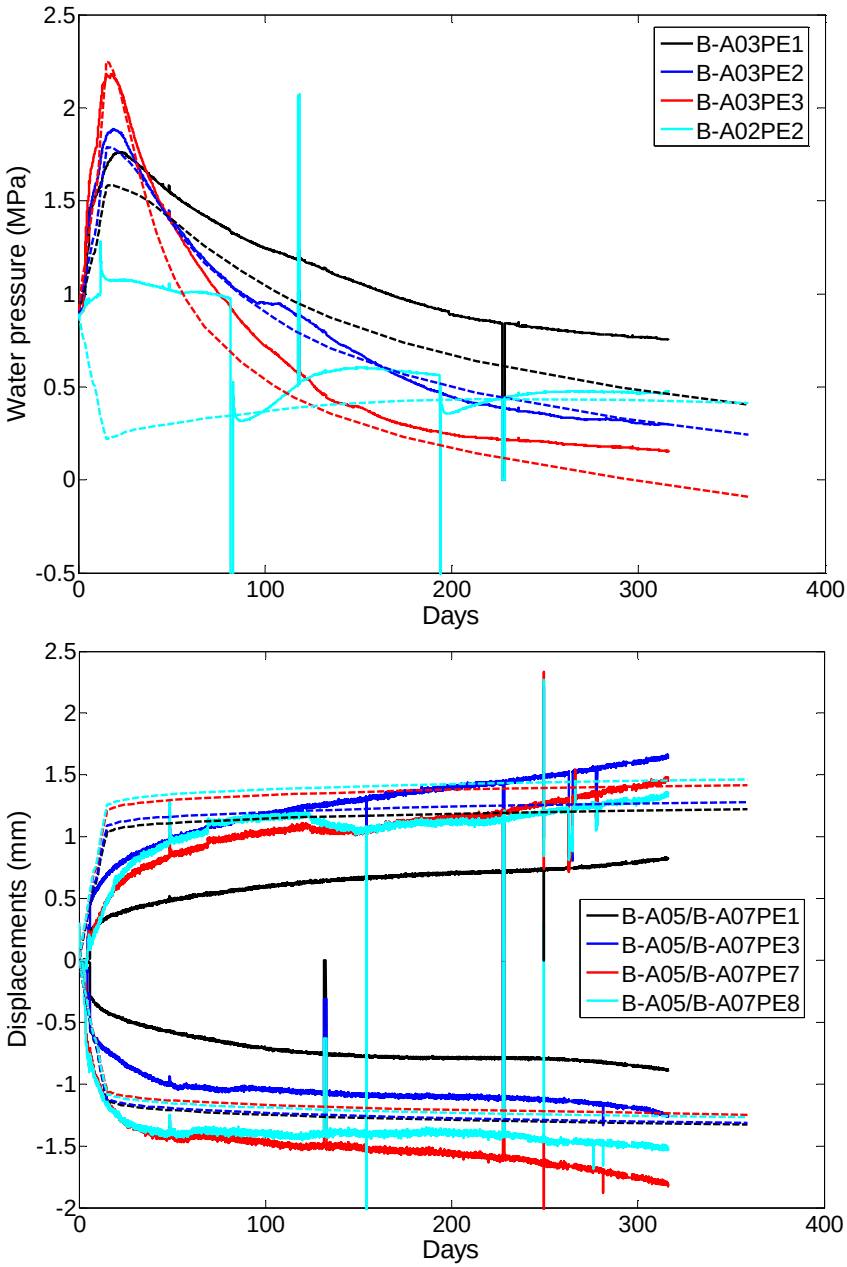

Figure 50: Final calibration of water pressure and displacements evolutions with time

Table 7: Calibrated Opalinus Clay parameters

Physical parameters			
Initial porosity	[-]	n_0	0.1
Volumic mass	[kg/m³]	ρ	2450
Water specific mass	[kg/m³]	ρ_w	1000
Water content	[%]	W	6.1
Fluid dynamic viscosity	[Pa.s]	μ_w	10^{-3}
Liquid compressibility coefficient	[MPa^{-1}]	$1/\chi_w$	5.10^{-4}
Mechanical parameters			
Young's modulus (in EDZ)	[GPa]	$E_{//}$	0.66
		$E_{\perp}$	0.5
Young's modulus (outside EDZ)	[GPa]	$E_{//}$	7
		$E_{\perp}$	3.5
Poisson's ratio	[-]	$\upsilon_{////}$	0.33
		$\upsilon_{//\perp}$	0.24
Shear modulus (in EDZ)	[GPa]	$G_{////}$	0.195
		$G_{//\perp}$	0.240
Shear modulus (outside EDZ)	[GPa]	$G_{////}$	2.8
		$G_{//\perp}$	1.3
Friction angle	[°]	$\varnothing_c$	20
Cohesion	[MPa]	$c_{0°}$	6.4
		$c_{45°}$	1.8
		$c_{90°}$	4.5
Dilatancy	[°]	ψ	0
Biot coefficient	[-]	b	0.6
Hydraulic parameters			
Initial intrinsic permeability (in EDZ)	[m²]	$k_{sat,//}$	2.10^{-15}
		$k_{sat,\perp}$	8.10^{-16}
Initial intrinsic permeability (outside EDZ)	[m²]	$k_{sat,//}$	$1.15\ 10^{-20}$
		$k_{sat,\perp}$	$4.65\ 10^{-21}$
Coefficients of the water retention curve	[MPa]	CSR1	5
	[-]	CSR2	1.2

5 Conclusions

The hydro-mechanical behaviour of Opalinus Clay around an excavated gallery has been numerically simulated through a 2D plane strain approach. To reproduce the dependency of the shear strength with the bedding orientation, an extended Drucker-Prager model with an anisotropic cohesion has been developed. The ability of that model to reproduce the behaviour of Opalinus Clay has been proved by numerical simulations of triaxial tests performed with different orientations of loading with respect to bedding plane and by numerical simulations of HGA microtunnel. However, analyses have put in evidence some numerical difficulties and the necessity to add complementary investigations on the presence of the main gallery, the presence of a tectonic fault or the creation of an excavation damaged zone around borehole. This has retarded the initial program, explaining why no numerical modelling relative to water and gas injection tests (subtasks 2 and 3) has been investigated.

Based on subtask 1 and the modelling of tunnel excavation, we have shown that the hydro-mechanical response of the Opalinus Clay around excavation is governed by four sources of anisotropy: the in-situ stress, the elastic modulus, the plastic yielding and the water permeability, keeping quite complex the global response of Opalinus Clay. Nevertheless, all the developments performed on HGA microtunnel numerical simulations show good agreement with available in-situ experimental measurements in term of displacement and water pressure evolutions.

6 References

Barnichon J.D. (1998). Finite element modelling in structural and petroleum geology. *PhD Thesis, Université de Liège.*

Ben Nasrallah S., Pere P. (1988). Detailed study of a model of heat and mass transfer during convective drying of porous media. *Int. J. Heat Mass Transfer*, 31(5): 957–967.

Bernier F., Li X.L., Bastiaens W., Ortiz L., Van Geet M., Wouters L., Frieg B., Blumling P., Desrues J., Viaggiani G., Coll C., Chanchole S., De Greef V., Hamza R., Malinsky L., Vervoort A., Vanbrabant Y., Debecker B., Verstraelen J., Govaerts A., Wevers M., Labiouse V., Escoffier S., Mathier J.F., Gastaldo L., Bühler Ch. (2007) *Fractures and self-healing within the excavation disturbed zone in clays (Selfrac)*. Final report, 5th EURATOM Framework Programme (1998 – 2002).

Bock H. (2001). *RA Experiment, Rock mechanics analyses and synthesis: Data report on rock mechanics*. Technical report 2000-02, Mont Terri Project.

Drucker D.C., Prager W. (1952). Solid mechanics and plastic analysis for limit design. *Quarterly of Applied Mathematics*, vol. 10(2), pp. 157-165.

Duveau G., Shao J.F. and Henry J.P. (1998). Assessment of some failure criteria for strongly anisotropic geomaterials. *Mechanics of cohesive-frictional materials*, vol. 3, pp. 1-26.

Gens A., Vaunat J., Garitte B., Wileveau Y. (2007). In situ behaviour of a stiff layered clay subject to thermal loading: observations and interpretation. *Geotechnique*, vol. 57(2), pp. 207–228.

Gerard P., Charlier R., Chambon R., Collin F. (2008) Influence of evaporation and seepage on the convergence of a ventilated cavity. Water Resour. Res., vol. 44: W00C02. doi: 10.1029/2007WR006500.

Ghezzehei T.A., Trautz R.C., Finsterle S., Cook P.J., Ahlers C.F. (2004) Modeling coupled evaporation and seepage in ventilated cavities. Vadose Zone J., vol. 3, pp. 806–818.

Graham J., Houlsby G.T. (1982) Anisotropic elasticity of a natural clay. *Géotechnique*, vol. 33(2), pp. 165-180.

Laloui L., François B. (2008). Benchmark on constitutive modeling of the mechanical behaviour of Opalinus Clay. *Mont Terri Project, Technical Report.*

Levasseur S., Charlier R., Frieg B., Collin F. (2010) Hydro-mechanical modelling of the excavation damaged zone around an underground excavation at Mont Terri rock laboratory. *Int. J. Rock Mech. Min. Sci.*, vol. 47(3), pp. 414-425.

Marschall P., Horseman S. and Gimmi T. (2005). Characterisation of Gas Transport Properties of the Opalinus Clay, a Potential Host Rock Formation for Radioactive Waste Disposal. *Oil & Gas Science and Technology – Rev. IFP*, vol. 60(1), pp. 121-139.

Martin C. D., Lanyon G. W. (2003) Measurement of in situ stress in weak rocks at Mont Terri Rock Laboratory, Switzerland. *Int. J. Rock Mech. Mining Sci.*, vol. 40(7–8), pp. 1077–1088.

Niandou H., Shao J.F., Henry J.P., Fourmaintraux D. (1997). Laboratory investigations of the mechanical behaviour of Tournemire shale, *Int. J. Rock Mech. Min. Sci.*, vol. 34, pp. 3-16.

Pietruszczak S., Mroz Z. (2001). On failure criteria for anisotropic cohesive-frictional materials. *Int. J. Numer. Anal. Meth. Geomech.*, vol. 25, pp. 509-524.

Pietruszczak S., Lydzba D., Shao J.F. (2002). Modelling of inherent anisotropy in sedimentary rocks. *Int. J. Solids and Structures*, vol. 39, pp. 637-648.

Trick T., Marschall P., Rösli U., Lettry Y., Bossart P., Enachescu C. (2007). Instrumentation for a gas path through host rock and along sealing experiment. *7th International Symposium on Field Measurements in Geomechanics.*

Wileveau Y. (2005). THM behaviour of host rock (HE-D) experiment: Progress report. *Part 1, Technical Report TR 2005-03. Mont Terri Project.*